

1 **Mixing and crystal scavenging in the Main Ethiopian Rift revealed by trace element**
2 **systematics in feldspars and glasses**

3
4 **Fiona Iddon^{1*}, Charlotte Jackson¹, William Hutchison², Karen Fontijn³, David M. Pyle³,**
5 **Tamsin A. Mather³, Gezahegn Yirgu⁴ and Marie Edmonds¹**

6
7 ¹ Department of Earth Sciences, University of Cambridge

8 ² School of Earth and Environmental Sciences, University of St Andrews

9 ³ Department of Earth Sciences, University of Oxford

10 ⁴ School of Earth Sciences, Addis Ababa University

11

12 Corresponding author: Fiona Iddon (fei20@cam.ac.uk)

13

14 **Key Points:**

- 15 • Alkali feldspars have variable trace element (Ba) concentrations, some far from
16 equilibrium with their carrier liquids (melts).
- 17 • Some feldspars are *antecrysts* (in equilibrium with a liquid on the line of descent, but not
18 the host melt), picked up from a crystal mush.
- 19 • Ignimbrites erupted during caldera-forming events are dominated by antecrysts, perhaps
20 scavenged from deep parts of the magma reservoir.

21

22

23 **Abstract**

24 For many magmatic systems, crystal compositions preserve a complex and protracted history
25 which may be largely decoupled from their carrier melts. The crystal cargo may hold clues to the
26 physical distribution of melt and crystals in a magma reservoir and how magmas are assembled
27 prior to eruptions. Here we present a geochemical study of a suite of samples from three
28 peralkaline volcanoes in the Main Ethiopian Rift. Whilst whole-rock data shows strong fractional
29 crystallisation signatures, the trace element systematics of feldspars, and their relationship to
30 their host glasses, reveals complexity. Alkali feldspars, particularly those erupted during caldera-
31 forming episodes, have variable Ba concentrations, extending to high values that are not in
32 equilibrium with the carrier liquids. Some of the feldspars are antecrysts, which we suggest are
33 scavenged from a crystal-rich mush. The antecrysts crystallised from a Ba-enriched (more
34 primitive) melt, before later entrainment into a Ba-depleted residual liquid. Crystal-melt
35 segregation can occur on fast timescales in these magma reservoirs, owing to the low viscosity
36 nature of peralkaline liquids. The separation of enough residual melt to feed a crystal-poor post-
37 caldera rhyolitic eruption may take as little as months to tens of years (much shorter than typical
38 repose periods of 300-400 years). Our observations are consistent with these magmatic systems
39 spending significant portions of their life cycle dominated by crystalline mushes containing
40 ephemeral, small ($< 1 \text{ km}^3$) segregations of melt. This interpretation helps to reconcile
41 observations of high crustal electrical resistivity beneath Aluto, despite seismicity and ground
42 deformation consistent with a magma body.

43

44 **Index Terms:**

45 1036, 1065, 1042, 8428, 8145

46 **Keywords:**

47 Peralkaline, Main Ethiopian Rift, crystal mush, crystal scavenging, antecryst, magma mixing

48

49 **1 Introduction**

50 Studies of magma storage and migration in the crust over the past decade have challenged
51 traditionally held views of magma chambers as large, molten melt bodies (see reviews by
52 Cashman & Giordano, 2014; Cashman & Sparks, 2013; Cashman et al., 2017). High-precision,
53 high-resolution geochemical studies of erupted volcanic products have revealed previously
54 undetected complexities at the mineral scale. Many systems show evidence of magmas being
55 stored, between eruptions, at near-solidus conditions for prolonged periods of time (e.g.
56 Bachmann & Bergantz, 2008; Cashman et al., 2017; Cooper & Kent, 2014). Heterogeneous
57 crystal cargoes in volcanic rocks, which are often not in equilibrium with their carrier liquids,
58 suggest that mixing may be ubiquitous. Crystal-rich mushes may be disrupted and disaggregated
59 prior to and during eruptions, leading to the accumulation of a range of diverse crystals in the
60 magma; e.g. Fish Canyon Tuff (Bachmann et al., 2002), Shiveluch Volcano (Humphreys et al.,
61 2008), Mount Hood (Cooper & Kent., 2014), and Yellowstone (Wotzlaw et al., 2014). Added to
62 these geochemical lines of evidence, geophysical imaging of the upper crust has often failed to
63 detect large bodies of melt beneath active volcanoes (e.g. Hübner et al., 2018; Manzella et al.,
64 2004; Samrock et al., 2015). This has led to suggestions that, in some circumstances, magmas

65 may be stored as melt-poor mush, which is expected to have a low electrical conductivity and
66 low V_p/V_s ratio (Chu et al., 2010; Miller & Smith, 1999; Steck et al., 1998; Zandt et al., 2003).

67 Many studies are published on the crystal cargoes of large magma reservoirs in
68 metaluminous, calc-alkaline magmatic systems; to date, there has been little attention paid to the
69 crystal cargoes of peralkaline magma reservoirs, despite their prevalence in continental rift
70 settings. There are few constraints on the architecture and dynamics of peralkaline magma
71 reservoirs, and little is known about the types of geophysical signals such magma bodies would
72 generate. Peralkalinity, defined as having an excess of alkalis with respect to aluminium (molar
73 $(\text{Na}_2\text{O}+\text{K}_2\text{O})/\text{Al}_2\text{O}_3 > 1$; Shand et al., 1927), has a strong influence on melt rheology, and thus
74 magma behaviour (Lanzo et al., 2013; Neave et al., 2012; Stevenson & Wilson, 1997). The
75 elevated alkali content of peralkaline melts, coupled with high dissolved halogen contents
76 (Barclay et al., 1996), results in peralkaline liquids having much lower viscosity (by 2 to 3 log
77 units) compared to their metaluminous counterparts, particularly at temperatures approaching the
78 solidus (di Genova et al., 2013). The low viscosity of peralkaline melts likely influences magma
79 reservoir processes. Crystal-melt segregation via settling and/or compaction within the crustal
80 storage system may occur faster than in metaluminous arc settings for similar melt SiO_2 contents
81 (Macdonald, 2012; Neave et al., 2012), and magma reservoirs may become more rapidly density-
82 stratified, hindering overturn and mixing (Blake & Ivey, 1986; Macdonald, 2012; Mahood &
83 Hildreth, 1986; Neave et al., 2012; Peccerillo et al., 2003).

84 The Main Ethiopian Rift (MER) is a northerly segment of the East African Rift system
85 (EARS) (**figure 1a**), a present-day example of continental rifting. Whole-rock compositions of
86 rift magmas are commonly bimodal (Boccaletti et al., 1995; Gasparon et al., 1993; Hutchison et
87 al., 2016c; Macdonald et al., 2011; Mazzarini et al., 2004; Peccerillo et al., 2003; Rooney et al.,
88 2012; Ronga et al., 2010; Trua et al., 1999). Alkali basalts erupt outside the calderas and along
89 faults (Mazzarini et al., 2013; Rooney et al., 2011), whilst peralkaline trachytes and rhyolites
90 dominate the eruptive products from axis-central volcanoes. Isotope and trace element
91 systematics of whole-rock material indicate the rhyolites are derived from protracted fractional
92 crystallisation of an alkali basalt parent (Giordano et al., 2014; Hutchison et al., 2016c;
93 Hutchison et al., 2018; Macdonald et al., 2011; Peccerillo et al., 2003). Modelling suggests that
94 the least evolved trachytes at Gedemsa Volcano (location shown in **figure 1b**) are generated after
95 ~70% fractional crystallisation of the basalts, and peralkaline rhyolite after an additional ~20%
96 (Peccerillo et al., 2003). The transition to peralkalinity in these magmas occurs after 80 to 85%
97 crystallisation, when the dominant crystallising phase changes from sodic plagioclase to alkali
98 feldspar (Bailey & Schairer, 1964; Barberi et al., 1974), causing the melt to evolve towards the
99 minimum in the $\text{Na}_2\text{O}-\text{K}_2\text{O}-\text{Al}_2\text{O}_3-\text{SiO}_2$ system (Carmichael & Mackenzie, 1963).

100 Despite seemingly simple whole-rock geochemical signatures, controlled by fractional
101 crystallisation, there is petrological and geochemical evidence for more complex magma
102 processing prior to eruptions at MER volcanic centres. For example, heterogeneous glass
103 compositions, zoned feldspar and clinopyroxene phenocrysts, and resorbed feldspar and olivine
104 phenocrysts have been cited as evidence for magma mixing at Boset-Bericha volcano
105 (Macdonald et al., 2011), whilst mingled glass compositions have been observed at Chefe Donsa
106 (Rooney et al., 2012) and intermediate-composition enclaves have been found in erupted
107 products from Aluto (Hutchison et al., 2016c) (locations shown in **figure 1b**). High Ba and Mn
108 concentrations in porphyritic trachytes from Gedemsa volcano (location shown in **figure 1b**)
109 have been linked to feldspar and fayalite accumulation, with mass balance calculations

110 suggesting a minimum of 10% crystal accumulation (Peccerillo et al., 2003). The resorbed nature
111 of some phenocrysts is consistent with an antecrystic nature (Peccerillo et al., 2003). The
112 petrology of these complex erupted products may encode information about how magmas are
113 stored and remobilised during eruptions, which may be relevant to interpreting geophysical data
114 acquired in the region. Significant portions of melt may be held in crystal-rich magma reservoirs,
115 ready to be remobilised and extracted (e.g. Bachmann & Bergantz, 2008; de Silva et al., 2008;
116 Ruprecht & Bachmann, 2010; Wark et al., 2007), but these melt regions can be difficult to detect
117 using geophysical techniques. For example, there is debate concerning the current state of the
118 magma reservoir beneath Aluto volcano. Seismic and deformation data, combined with
119 geobarometric estimates and Holocene eruptive frequency (Fontijn et al., 2018; Hutchison et al.,
120 2016a; Hutchison et al., 2016c; Wilks et al., 2017), point to the existence of a shallow magma
121 storage system. However, magnetotelluric methods fail to identify a volume of enhanced
122 electrical conductivity in the crust (Hübner et al., 2018; Samrock et al., 2015) that might indicate
123 the presence of partial melt (e.g. Pous et al., 1999; Hoffman-Rothe et al., 2011; Schilling &
124 Partzsch, 2001). In contrast, enhanced electrical conductivity, interpreted as the presence of
125 crustal melt, has been imaged in similar surveys at the nearby Boset-Bericha volcano (Whaler &
126 Hautot, 2006).

127 We hypothesise that melt-poor mush may dominate magma reservoir storage systems beneath
128 central volcanoes in the MER, and that this mush may be efficiently constructed in peralkaline
129 magmatic systems due to their unique rheological characteristics. To test this hypothesis we
130 undertake a systematic comparison between whole-rock, glass and feldspar compositions for a
131 suite of samples from three peralkaline MER volcanoes, Aluto, Kone, and Fentale (locations
132 shown in **figure 1b**). We focus on Ba, as it partitions strongly into alkali feldspars, the
133 overwhelmingly dominant crystallising phase in evolved peralkaline magmas; and on Zr, a
134 highly incompatible element in peralkaline melts and a useful proxy for fractional crystallisation.
135 We evaluate the extent to which the crystal cargo is in equilibrium with its carrier liquid by
136 comparing the results from the natural samples with experimental partitioning data for Ba using
137 models of fractional crystallisation generated from RhyoliteMELTS (Gualda et al., 2012).
138 Models of crystal settling and compaction (Bachmann & Bergantz, 2004) are used to assess the
139 degree of influence of peralkaline liquid rheology on timescales of crystal-melt segregation
140 processes. Finally, inferences about the types of geophysical signals such magma bodies would
141 generate are made, helping to inform future volcanic monitoring activities along the MER.

142

143 **2 Geological Setting**

144 The MER is part of the EARS (**figure 1a**), a continental rift between the Nubian and
145 Somalian plates (see reviews by Corti, 2009; Ebinger, 2005). Extending in a NNE-SSW direction
146 from the Afar to the Turkana depression (Mohr, 1983; WoldeGabriel et al., 1990), the MER is
147 currently undergoing active east-west extension of $\sim 5 \text{ mm yr}^{-1}$ (Saria et al., 2014). Extension was
148 initially accommodated by displacement along NE-SW trending faults (Bonini et al., 2005;
149 WoldeGabriel et al., 1990). Since 2 Ma, strain has largely been accommodated on the Wonji
150 Fault Belt (WFB) (Corti, 2009) and recent geodetic data confirms that 80% of the current strain
151 is accommodated on the WFB (Bilham et al., 1999). The WFB is a group of short N-NE trending
152 en-echelon faults that lie within a $\sim 15 \text{ km}$ wide axial zone in the MER (Agostini et al., 2011;
153 Keir et al., 2006; Keir et al., 2015). Pleistocene and Holocene volcanism has been focused within

154 tectono-magmatic segments along the rift that are co-located with the WFB (Abebe et al., 2007;
155 Corti, 2009; Fontijn et al., 2018; Keir et al., 2006; Keir et al., 2015; Rooney et al., 2011).

156 Aluto, Kone, and Fentale are peralkaline caldera complexes located in the MER (**figure**
157 **1b and 1c, 1d, and 1e, respectively**). Whole-rock compositions, petrographic descriptions and
158 geochronology for Aluto volcanic products are presented by Hutchison et al. (2016c), and for
159 Fentale by Gibson (1974) and Giordano (2014). In contrast, there are few data available for Kone
160 volcano. Cole (1968) and Rampey et al. (2010) provide descriptions of major map units,
161 however previous petrographic and geochemical investigations have largely been limited to a
162 Plinian eruptive deposit known as the Gubisa formation (**figure 1d**, Rampey et al., 2014), with
163 some limited data also available on basalts that infill the caldera structure (Furman et al., 2006;
164 Rooney et al., 2007; Rooney et al., 2012).

165 The Kone central volcanic complex comprises the older ~ 95 km² caldera (Birenti), and
166 the younger, 22 km² Kone caldera with a small embayment of 2 km² known as the Korke caldera
167 (Rampey et al., 2010, 2014) (**figure 1d**). Both structures are thought to have formed during a
168 multi-eruption event, with the later Kone and Korke calderas developing during a series of 3-4
169 sub-Plinian and Plinian eruptions (Rampey et al., 2010, 2014). The Gubisa formation is
170 associated with the formation of the Kone caldera (**figure 1d**); deposits are up to 60 m thick with
171 a minimum volume of 3.2 km³ (Rampey et al., 2014). Deposits associated with caldera-forming
172 events are well preserved and dominate surface exposure at the Kone volcanic complex.
173 Trachytic and rhyolitic lava domes and associated minor deposits of pumice preceded and
174 followed the caldera-forming events. There are no dates available for Kone eruptions, though
175 tectonically-controlled basaltic lava effusion, exploiting the join between the Kone and Korke
176 calderas and filling both structures (**figure 1d**), likely represents the most recent volcanism
177 (Fontijn et al. 2018; Rampey et al., 2010, 2014). Basaltic scoria cones and fissure lavas are also
178 present to the Southwest and Northeast (**figure 1d**), aligned with the WFB (Rampey et al., 2010,
179 2014).

180 Fentale volcano is the northernmost silicic centre in the MER, located at the junction with
181 the Afar region (**figure 1b**) (Gibson 1967, 1969, 1970, 1974). It is a 600 m high stratocone built
182 of silicic lava flows and rare tephra horizons, with a 300 m deep summit caldera known as Tilik
183 volcano (**figure 1e**) (Gibson 1967, 1969, 1970, 1974; Giordano et al., 2014; Kidane et al., 2009;
184 Webster et al., 1993). The 30 km² caldera is roughly elliptical in shape and is thought to have
185 formed during an explosive eruption between 0.17 and 0.151 Ma (Williams et al., 2004). The
186 deposits of this eruption are widespread, forming intensely welded tuffs up to 30 m thick,
187 blanketing the plain and covering the slopes of the earlier edifice (**figure 1e**) (Giordano et al.,
188 2014). Post-caldera volcanism consists largely of obsidian lava flows from vents within the
189 caldera itself and on the volcano's flanks, as well as from fissures along the rim (Acocella et al.,
190 2002; Gibson 1967, 1969, 1970, 1974; Fontijn et al., 2018; Webster et al., 1993; Williams et al.,
191 2004). Minor post-caldera explosive episodes have also occurred, with scattered pumice
192 observed on the edifice slopes (Fontijn et al., 2018) and a significant pumice cone on the southern
193 flank. Similar to Kone, the most recent activity was mafic, primarily on the southwestern side of
194 the volcano, where the WFB intersects the Fentale complex. Here fissure lavas cover a 3 km²
195 area (**figure 1e**) and have been dated to ~ 1810 -1820 based on oral tradition (Harris, 1844).

196 At Aluto volcano at least 8-21 km³ of welded, green rhyolitic ignimbrites and trachytic
197 tuffs erupted during the formation of a 42 km² caldera structure at ca. 300 ka. It is not possible to
198 identify if this was a singular or multiple-eruption event, due to the generally poor surface

199 exposure of these deposits (Hutchison et al., 2015, 2016c). Post-caldera volcanism has been
 200 ongoing since at least ca. 60 ka, possibly after a significant hiatus (Hutchison et al., 2016c), and
 201 dominates the exposed volcanic rocks (**figure 1c**). These post-caldera eruptions are thought to
 202 typically initiate with explosive eruptions, building small pumice cones and/or emplacing
 203 pyroclastic density currents, before effusive eruptions of obsidian coulées (Hutchison et al.,
 204 2016c). Basaltic volcanism is largely confined to scoria cones and fissure lavas to the North-East
 205 of the main edifice (**figure 1c**). Hutchison et al. (2016c) suggest a relationship between the
 206 basalts and the caldera system based on proximity and comparable surface weathering of
 207 eruptive products, though the cones are strongly aligned with the WFB. It is hypothesised that
 208 silicic magma chambers in the MER act as mechanical density filters, forcing mafic melts to
 209 erupt externally to caldera margins (Peccerillo et al., 2003). The most recent dated eruption
 210 occurred several hundred years ago (0.4 ± 0.05 cal ka BP; Hutchison et al., 2016c), and at least
 211 25 eruptions are identified in the Holocene period (Fontijn et al. 2018).

212 Episodes of ground deformation, thought to have a magmatic origin, have occurred at
 213 Aluto volcano over at least the past decade (Biggs et al., 2011; Hutchison et al., 2016a). InSAR
 214 observations show periods of rapid inflation followed by periods of long-term subsidence. The
 215 inflation is thought to reflect fluid injection into the roof zone of a magma storage region, whilst
 216 subsidence was interpreted as magmatic degassing and depressurisation of the hydrothermal
 217 system (Hutchison et al., 2016a). The deformation is consistent with a source at ~5 km depth.
 218 Seismicity has been identified between 2-9 km depth, which also reflects magmatic fluids
 219 causing elastic deformation (Wilks et al., 2017). However, magnetotelluric methods fail to
 220 identify a volume of enhanced electrical conductivity at this depth in the crust (Hübert et al.,
 221 2018; Samrock et al., 2015) that might indicate the presence of partial melt (e.g. Pous et al.,
 222 1999; Hoffman-Rothe et al., 2011; Schilling & Partzsch, 2001).

223 3. Analytical Techniques

224 The Aluto samples used in this study were collected by Will Hutchison between 2012 and
 225 2014. The Kone samples were collected by both Michael Rampey between 2001 and 2003 and
 226 Karen Fontijn and Keri McNamara in November 2015. The Fentale samples were collected by
 227 Fiona Iddon, Jonathan Hunt, and Abate Assen in October 2017. Caldera-forming ignimbrites,
 228 post-caldera silicic lava and pumice, and later post-caldera basaltic lava and scoria were
 229 collected at each site. Where available pre-caldera silicic lava and pumice and pumice associated
 230 with caldera forming episodes was also utilised in the study. See **table 1 and 2** for all sample
 231 locations, refer to Hutchison et al. (2016c) for full details on the Aluto samples.

232 Kone and Fentale samples were trimmed to access clean regions and then crushed and
 233 milled to produce powders. X-ray fluorescence spectrometry (XRF) analysis was used to acquire
 234 whole-rock major and trace element compositional data on fusion beads and powder pellets
 235 respectively. Loss on ignition (LOI) was determined at 950 °C . Data was acquired at the
 236 Department of Geology at the University of Leicester using a PANalytical Axios-Advanced XRF
 237 spectrometer. Precision of 5% for majors (11% for MnO, 8% for P₂O₅) and 6% for trace
 238 elements was achieved using a range of secondary standards; Ba showed a precision of 4% and
 239 Zr a precision of 1%. An accuracy of 7% (11% for P₂O₅) was achieved for majors and 10% for
 240 trace elements; Ba was analysed with an accuracy of 9% and Zr an accuracy of 6%. Standards
 241 compilations can be found in **supplementary material**. Precision and accuracy (in %) were
 242 calculated as $100 \frac{\sigma}{\bar{x}}$ and $100 \frac{(\bar{x} - x_{ref})}{x_{ref}}$ respectively.

243 Polished sections (30-50 μm thick) were used for petrographic analysis and geochemical
244 analyses of phenocryst phases. The Quanta-650F Scanning Electron Microscope (SEM) at the
245 Department of Earth Sciences of the University of Cambridge was used to acquire back-scattered
246 electron (BSE) images and maps to assess sample crystal fraction and to provide microtextural
247 information. A 15 kV beam and 4 μm spot was used for Aluto samples; a 10 kV beam and 5 μm
248 spot was used for Kone samples (images were acquired by different operators). QEMSCAN
249 software was used for quantitative analysis, and to assess the major phases present and major
250 element zoning. The QEMSCAN software creates phase assemblage maps from data acquired
251 from a combination of low-count energy-dispersive X-ray spectra (EDX) and BSE brightness
252 and X-ray count information. Fiji software, an open source image processing package
253 (Schindelin et al., 2012), was used to quantitatively assess crystal fraction.

254 Chemical compositions of the main phases and the matrix glass were measured using a
255 Cameca SX-100 Electron Probe Micro-Analyser (EPMA) at the University of Cambridge. An
256 accelerating voltage of 15 kV was used for all analysis. A defocused beam of 10 μm and a
257 current of 10 nA was used for glass analyses. A precision and accuracy of 6% for
258 major elements (precision of 10% for MnO and 9% for P_2O_5 ; accuracy of 8% for MnO and 41%
259 for P_2O_5) was achieved using a range of secondary standards. Plagioclase and alkali feldspar
260 were also measured using a 10 nA beam but with a defocused beam of 5 μm . Pyroxenes were
261 measured using a 1 μm sized beam with a current of 10 nA. For all phases some trace elements
262 were measured using a second condition with a higher current voltage of between 40 and 100
263 nA. Counting times of 10-30 s were used for major elements, 40-90 s for trace elements and 10-
264 12 s for alkalis. Where the beam current was increased to 100 nA, for example for the
265 measurement of Ba and Sr within feldspars, counting times of up to 400 s were used. A precision
266 of 6% and an accuracy of 3% for major elements (precision of 31% for TiO_2 and 16% for K_2O ;
267 accuracy of 19% for TiO_2 and 8% for K_2O) was achieved using a range of secondary standards.
268 Standards compilations can be found in **supplementary material**.

269 Trace element analysis of matrix glasses was acquired by secondary ion mass spectrometry
270 (SIMS) using a Cameca ims-4f ion probe at the School of Geosciences at the University of
271 Edinburgh. Glass chips were hand-picked from crushed material and mounted in epoxy blocks,
272 which were then gold-coated. A 25 mm square area was rastered with a low beam current prior
273 to analysis, to remove the gold coating and any contamination. A range of standards was used to
274 construct a robust calibration and analysed at the beginning and end of every session to assess
275 data quality. Precision of 4% and accuracy of 7% was achieved for all trace elements; Ba was
276 measured with a precision of 1% and an accuracy of 7%; Zr with a precision and accuracy of
277 2%. Standards compilations can be found in **supplementary material**.
278

279 **4 Results**

280 4.1 Petrographic descriptions

281 4.1.1 Alkali basalt

282 The alkali basalts are present as both porphyritic seriate lava and scoria (**figure 2a**).
283 Phenocrysts are typically up to a few mm in size, and represent from 5.5 to 26 absolute volume
284 % (vol%) of the scoria samples and up to 45 vol % of the lava samples. Phases include
285 plagioclase, olivine and augite (modal proportions of the phenocrysts of 78%, 22% and 0% for
286 the lavas, and 40%, 35% and 25% for the scoria). Glomerocrysts are common, at up to 4 mm

287 across they mainly comprise olivine and plagioclase, although clinopyroxene (**figure 2a**) is
288 particularly common in the scoria. Zoning is present in all phases (**figure 2a**), particularly
289 associated with the glomerocrysts. Olivine and plagioclase phenocrysts show normal zoning,
290 with rare occurrences of reverse-zoned olivine rims. Augite phenocrysts show oscillatory zoning.
291 Chrome spinels are generally present in the groundmass of both lavas and scoria, and as
292 inclusions within the phenocrysts.

293

294 4.1.2 Caldera-forming eruptions

295 Large-volume ignimbrite eruptions are associated with caldera-forming phases at Aluto,
296 Kone and Fentale (Fontijn et al., 2018; Gibson, 1967, 1970, 1974; Giordano et al., 2014;
297 Hutchison et al., 2016c; Rampey et al., 2010, 2014). Samples selected for study are all intensely
298 welded. Ignimbrite bulk compositions straddle the trachytic to rhyolitic boundary (**figure 3a**) and
299 are crystal-rich, with phenocrysts accounting for 17 to 35 absolute volume % (**figure 2b and 2c**).
300 The crystal population is dominated (up to 85 modal % proportion of the phenocrysts) by broken
301 euhedral feldspars up to 3 mm in size, which vary from oligoclase to anorthoclase to sanidine,
302 with the former more abundant in the less evolved samples, the latter in the most evolved (**figure**
303 **2b and 2c**). Some feldspars display normal zoning, with plagioclase cores (**figure 2b**);
304 occasional andesine (up to 5 modal %) is also present. Other phases include fayalite (up to 5
305 modal % in less evolved samples), with alteration rims, fractured quartz (up to 25 modal % in
306 more evolved samples), rounded or elongate aegirine-augite (up to 10 modal %) and aenigmatite
307 (up to 10 modal %). Most of these phases are up to 0.5 mm in size, but can reach up to 2.5 mm in
308 size in some cases. The phenocrysts can form a glomeroporphyritic texture, with clots up to 5
309 mm in size (**figure 2b and 2c**), set in a variably devitrified groundmass. Fe-Ti oxides are present
310 as microphenocrysts, 0.1-0.2 mm in size, clustering in and around the glomerocrysts (**figure 2b**).
311 Xenoliths of rhyolite and trachyte lava are common, particularly in rhyolitic ignimbrites, as are
312 finely crystalline fiamme and collapsed vesicles (**figure 2c**). The unwelded pumiceous fall
313 material, associated with caldera-forming eruptions, has a similar phase assemblage to the
314 rhyolitic ignimbrites and shows similar textures (**figure 2d**), although it has a lower phenocryst
315 content (<10 vol %).

316

317 4.1.3 Pre and post-caldera eruptions

318 Felsic lava and pumice is erupted during pre- and post-caldera phases. Samples selected
319 for study include pre-Birenti caldera, pre-Kone caldera and post-Kone caldera lava from Kone,
320 pre- and post-caldera lava from Fentale and post-caldera lava and pumice from Aluto. Trachytic
321 lava, and occasional rhyolite lava, contain up to ~30 vol % phenocrysts (**figure 2e**), dominated
322 by euhedral sanidines (>70 modal %) up to 3 mm in size, and small rounded quartz crystals (up
323 to 25 modal %) 0.2-0.3 mm in size. Aegirine-augite (<2.5 modal %) up to 2 mm in size, and
324 fayalite (<2.5 modal %) up to 3 mm in size, with thick alteration rims, complete the phase
325 assemblage. Glomeroporphyritic crystal clots are common (**figure 2e**). The fine-grained
326 (containing crystals up to 10 μ m in size) groundmass is made up of a similar assemblage. The
327 rhyolite lava is dominantly aphyric, or crystal-poor porphyritic obsidian with <10 vol % crystals
328 held in a glassy groundmass (**figure 2f**). The phase assemblage is made up by euhedral
329 phenocrysts of sanidine (70 modal %), rounded quartz (15 modal %), and elongate or rounded
330 aegirine augite and aenigmatite (7 modal %), all up to 1 mm in size. Granophyric intergrowths of

331 quartz and alkali feldspar are common (**figure 2f**). At up to 2.5 mm in size, these intergrowths
332 appear to nucleate around a grain showing dissolution textures, and can contain inclusions of
333 aegirine-augite. They may represent growth during rapid undercooling of melt compositions that
334 are under-saturated with respect to quartz (Gleeson et al., 2017; Lowenstern et al., 1997). The
335 glass matrix of the rhyolites contains aligned microlites of alkali feldspar and aegirine augite.
336 Post-caldera pumice deposits are similar in assemblage and petrographic texture to the post-
337 caldera rhyolite lavas, though generally have lower phenocryst contents (closer to aphyric).

338

339 4.2 Whole-rock and glass compositions

340 4.2.1 Major elements

341 Whole-rock compositions for Kone and Fentale are presented in **table 1 and provided in**
342 **supplementary 12 and supplementary 13**, glass compositions for Aluto, Kone and Fentale are
343 presented in **table 2** and provided in **supplementary 14**. Whole-rock compositions for Aluto
344 volcanic products are presented by Hutchison et al. (2016c) and are highlighted by fields marked
345 out by dashed lines. Rocks were classified using the total alkalis-silica (TAS) diagram (**figure**
346 **3a**) after LeBas et al. (1986), and the $\text{FeO}_t - \text{Al}_2\text{O}_3$ diagram (**figure 3b**) after Macdonald (1974).
347 There is a large range in silica content across the sample suite, although rocks of intermediate
348 composition are absent, the data show a clear gap in compositions between ~50 to 60 wt% SiO_2 ,
349 excepting rare examples of enclaves from Aluto (Hutchison et al., 2016c). All of the evolved
350 samples are peralkaline, with most classified as pantellerites based on their high FeO
351 concentrations (**figure 3b**; Macdonald, 1974). Some Aluto trachytic ignimbrites appear
352 comenditic due to their raised Al_2O_3 contents. The mafic samples have a transitional composition
353 and straddle the alkaline-subalkaline divide of Irvine and Baragar (1971) (**figure 3a**).

354 Both the glass and whole-rock data show that increasing SiO_2 content correlates with an
355 increase in alkalis and a decrease in ferromagnesian, Ca and Ti oxides (**figure 4**). This trend is
356 indicative of protracted fractional crystallisation controlled by removal of olivine, clinopyroxene,
357 plagioclase, Fe-Ti oxide, quartz, alkali feldspar and aenigmatite (in approximate order of
358 appearance). K_2O shows a smooth, largely linear increase (**figure 4g**). Al_2O_3 shows flat but
359 scattered levels before a step-change at ~68 wt. % SiO_2 , where it decreases to 7.5–12 wt. % in
360 the pantellerite samples, reflecting the dominance of alkali feldspar fractionation (**figure 4a**).
361 Na_2O shows an increasing trend with SiO_2 up to the trachytic compositions, then displays
362 considerable variation (2.5–7 wt. %) within the pantellerites (**figure 4f**). The variation in Na_2O
363 after ~70 wt.% SiO_2 reflects the dominance of alkali feldspar as the fractionating phase, though it
364 should be noted that glass alteration and Na loss may also be important. By comparing the FK/A
365 indicator of peralkalinity (mol (Fe+K)/Al) to that of the agpaite index (A.I.- mol (Na+K)/Al),
366 several Kone samples, namely the silicic glasses, are identified as likely to have undergone Na
367 loss (see **supplementary 1**) (White et al., 2003). Hutchison et al. (2016c) examined Na loss at
368 Aluto in samples collected from isolated pumice cones that would have been located at the edge
369 of the lake during lacustrine high stands, leading them to suggest that post-emplacement
370 alteration processes (e.g., leaching by surface water interaction) may be the causal factor. Na loss
371 has also been identified in pumice from Rungwe, Tanzania, Fontijn et al. (2013) suggest that the
372 combination of high vesicularity, increasing exposed surface area, and the climate contributes to
373 the alteration.

374 Whilst the glass and whole-rock data are generally tightly coupled, the glass data shows
375 slightly lower MgO and FeO, and higher TiO₂ and K₂O at the mafic end of the spectrum, and
376 higher SiO₂ and Na₂O at the silicic end of the spectrum, particularly compared to whole-rock
377 analyses of the crystal-rich ignimbrites. This likely reflects the presence of retained, large olivine
378 phenocrysts in the basalts, and alkali feldspar phenocrysts in the pantellerites. Peralkaline melts
379 become increasingly sodic as they evolve due to the ‘orthoclase effect’ (Bailey & Schairer,
380 1964). Gibson (1974) identified significant geochemical variation between Fentale pre- and post-
381 caldera pantellerites, this study replicates that with post-caldera samples showing higher SiO₂
382 and lower TiO₂, FeO, MnO contents noted in both the whole-rock and glass data. No such
383 pattern was observed for the Kone samples.

384 Best-fit RhyoliteMELTS models (Gualda et al., 2012) for Kone and Fentale were
385 determined using least squares residual analysis (following the method of Gleeson et al., 2017),
386 these are plotted as solid lines, along with the model for Aluto determined by Gleeson et al.
387 (2017) (**figure 3 and 4**). The models provide a good first-order fit to the geochemical data, but
388 deviation is observed for more evolved (pantelleritic) compositions. There is a departure of the
389 model from FeO, CaO, Na₂O and P₂O₅ glass and whole-rock compositions (**figures 4c, 4e and**
390 **4h**) and consequently the model overestimates peralkalinity substantially for the rhyolites with
391 SiO₂ > 70 wt%. Over-prediction of P₂O₅ and CaO is likely related to inaccuracies in the
392 stabilisation of apatite and other mineral phases for which Rhyolite-MELTS is not calibrated
393 (Rooney et al., 2012). Under-prediction of FeO content reflects the limited constraint on
394 aenigmatite stability (Hutchison et al., 2018). Rooney et al (2012) highlight the lack of
395 experimental constraints on the stability of F-bearing phases in thermodynamic models for
396 peralkaline systems.

397

398 4.2.2 Trace Elements

399 The co-variation of selected trace elements with Zr, which is highly incompatible in
400 peralkaline melts (**figure 5a**), is shown in **figure 5**. Compatible elements show a negative
401 correlation with Zr (**figure 5b and 5c**); incompatible elements show a positive correlation.
402 Incompatible-incompatible trace element diagrams (**figure 5d-g**) show linear positive trends that
403 pass through the origin, and are consistent with the most evolved compositions at Aluto, Kone,
404 and Fentale being derived from a mafic parent similar to those sampled. Incompatible element
405 ratios such as Rb/Nb (**figure 5h**) do not show significant variability across the sample suite.
406 Rb/Nb ratios are generally lower in the sample suite than that of the Precambrian crustal rocks
407 (Peccerillo et al., 1998), which likely represent a component of the basement rocks.

408 Glass and whole-rock compositions are tightly coupled. Ba contents deviate from the
409 other elements analysed, showing an increase in concentrations up to trachytic compositions, and
410 then considerable variation (12–850 ppm) within the pantellerites (**figure 5c**), marking the
411 appearance of alkali feldspar as a major fractionating phase. There is no clear relationship
412 between the Ba concentrations observed in the whole-rock and in glass (**figure 5c**). Given the
413 textural evidence of glomerocrystic clots of feldspar phenocrysts this may indicate accumulation
414 of trace-element-enriched feldspar crystals (see section 5.3). Again, this study confirms the result
415 of Gibson (1974), identifying differences between the trace element geochemistry of Fentale pre-
416 and post-caldera pantellerites. Post-caldera samples have higher whole-rock and glass

417 concentrations of incompatible elements such as Y, Nb, La, and Rb, but lower concentrations of
418 Ba. No such pattern was observed for the Kone samples.

419

420

421 4.3 Feldspar compositions

422 Plagioclase compositions in the Aluto samples include bytownite and labradorite (An₅₅₋₈₁;
423 Ab₄₂₋₁₈; Or₁₋₃), whilst Kone samples are dominated by bytownite (An₈₀₋₈₄; Ab₁₉₋₁₅; Or₀₋₁) (**figure**
424 **6**). Aluto trachytes contain feldspars that straddle the oligoclase/anorthoclase boundary (An₅₋₄₂;
425 Ab₇₇₋₅₆; Or₃₋₂₄), with some rare andesine cores. Kone and Fentale samples contain minor amounts
426 of these feldspars (An₁₁₋₂₀; Ab₇₃₋₇₂; Or₈₋₁₈). Alkali feldspars at Aluto are predominantly sanidine
427 (An_{0.1-0.4}; Ab₆₈₋₅₀; Or₃₂₋₆₅), whilst at Kone and Fentale they straddle the anorthoclase/sanidine
428 boundary (An_{0.1-3}; Ab₇₆₋₅₄; Or₂₄₋₄₆). Whilst some anorthoclases in both Kone and Aluto caldera-
429 forming eruptive deposits display normal zoning, with more albitic cores (**figure 2b**), most show
430 no apparent zoning (**figure 2c-f and 7a and 7b**); the range from core to rim is typically <3 mol%
431 for Or and Ab. The feldspar analyses can be found in **table 3** and **supplementary 15 and**
432 **supplementary 16**.

433 The predicted feldspar compositions from the best-fit RhyoliteMELTS models (Gleeson
434 et al., 2017; Gualda et al., 2012) are shown plotted as solid lines on **figure 6**. They provide a
435 good first-order fit to the geochemical data, following the smooth curve displayed by the
436 observed plagioclase data closely. However, RhyoliteMELTS fails to accurately predict the
437 composition of the alkali feldspars, over-predicting Or contents. The modelled fractionation of
438 more potassic feldspars results in RhyoliteMELTS overestimating peralkalinity, as the influence
439 of the orthoclase effect (Bailey & Schairer, 1964) is inflated.

440 Ba concentrations were used to assess trace element variation in the feldspars from the
441 evolved rocks as Ba partitions strongly into the mineral phase and, unlike Sr, was observed
442 above detection limits in most cases for the alkali feldspars. Data is presented in **table 3**. The
443 oligoclase and anorthoclase plagioclase feldspars typically contain the highest Ba concentrations,
444 reaching >4000 ppm Ba. Alkali feldspar Ba contents are highly variable at the individual sample
445 scale for each of the volcanoes investigated, with an average standard deviation of 339 ppm for
446 the Aluto samples, 266 ppm for the Kone samples, and 453 ppm for the Fentale samples. It
447 should be noted that every sample also contained feldspars with Ba concentrations below the
448 detection limits so the actual variation is larger. Individual samples contain feldspars with a
449 standard deviation in Ba concentration of up to 853 ppm, with Ba concentrations varying
450 between several hundred ppm and >4000 ppm. Variation in Ba concentrations tends to be
451 greatest within the samples erupted during caldera-formation; and these samples also contain the
452 most crystals with Ba concentrations above detection limits. Evidence for zoning was limited
453 within the alkali feldspars (**figure 7a and b**). Where zoning in major elements exists there is no
454 systematic change in Ba contents from core to rim (**figure 7a**). The limited amount of zoning
455 observed may have been acquired from a range of processes (i.e., feldspar growth in a
456 progressively evolving liquid, diffusive re-equilibration of crystals scavenged from a
457 geochemically distinct region). Only the rims, and their relationship to their carrier liquids, are
458 examined further in this study (note that in most cases the rims and cores are identical; **Figure**
459 **7**).

460

461 **5 Discussion**

462 5.1 Magma compositions are dominated by a fractional crystallisation signature

463 As has been proposed in previous studies (e.g. Giordano et al., 2014; Hutchison et al.,
464 2016c; Hutchison et al., 2018; Macdonald et al., 2011; Peccerillo et al., 2003), the whole-rock
465 and glass data are consistent with pantelleritic magmas being derived via extreme fractional
466 crystallisation of a basaltic parental melt. Following the method of Gleeson et al. (2017) for
467 Aluto (for full details see **supplementary 2 and 3**), least squares residual analysis was used to
468 find the best fit RhyoliteMELTS models (Gualda et al., 2012) for Kone and Fentale, using
469 basalts from these volcanoes as starting compositions (samples MER133A and F12). There are a
470 number of initial conditions which appear to provide a reasonably good match to the
471 compositional data, however results of the statistical analysis indicate that fractional
472 crystallisation at low pressure conditions (100 MPa), f_{O_2} at the QFM-QFM+1 buffer, and an
473 initial water content of ~1 wt% offer the best-fit RhyoliteMELTS models for Kone and Fentale
474 volcanoes. This is consistent with the best-fit model presented by Gleeson et al. (2017) for Aluto,
475 and with findings for other peralkaline centres along the MER and globally (e.g. Barberi et al.,
476 1975; Gasparon et al., 1993; Hutchison et al., 2018; Peccerillo et al., 2003; Neave et al., 2012;
477 Rooney et al., 2012).

478 Some authors have suggested that peralkaline magmas may be generated by melting of
479 pre-existing basaltic rocks (Beard & Lofgren, 1991; Garland et al., 1995; Hay & Wendlandt,
480 1995; Thy et al., 1990). However, trace element ratios are constant through the differentiation
481 suite and are also much lower than those of the local Precambrian crust (**figure 5h**). Peccerillo et
482 al. (2003) suggest that partial melting of crustal rocks would tend to increase melt large ion
483 lithophile and high field strength element ratios (LILE/HFSE, e.g., Rb/Nb) making it unlikely
484 that there has been significant contribution from crustal assimilation. Hutchison et al. (2018)
485 used Sr-Nd-O isotope systematics to rule out major crustal assimilation at both Kone and Aluto,
486 consistent with these findings.

487

488 5.2 Implications for our understanding of Daly Gap formation

489 There is a total absence of eruption deposits at Kone and Fentale with the intermediate
490 magma compositions which are predicted to form during protracted fractional crystallisation.
491 This compositional gap is often referred to as the 'Daly Gap' (Daly, 1925) and has also been
492 noted at Aluto (Gleeson et al., 2017; Hutchison et al., 2016c) where only rare enclaves, thought
493 to be the product of magma mixing (Hutchison et al., 2016c) have intermediate compositions.
494 The 'Daly Gap' has been observed at other sites along the MER (Peccerillo et al., 2003; Ronga et
495 al., 2009; Rooney et al., 2012), and at other peralkaline systems globally (Neave et al., 2012;
496 White et al., 2009). The 'Daly Gap' is often used to argue against derivation of peralkaline
497 liquids by protracted fractional crystallisation (e.g. Chayes, 1963; 1977). Despite this challenge,
498 the feldspar data collected for Aluto, Kone and Fentale preserve evidence for crystallisation of
499 magmas of intermediate composition somewhere in the storage system. The smooth change in
500 feldspar major element compositions observed in the samples analysed is further supported by
501 the RhyoliteMELTS simulations of fractional crystallisation, which closely replicate plagioclase
502 feldspar evolution (**figure 6**). The majority of the andesine and oligoclase analyses were taken

503 from resorbed feldspar cores, rimmed by more potassic compositions (**figure 2b and 2c**),
 504 providing geochemical evidence for crystallisation of intermediate magmas prior to melt
 505 evolution. White et al. (2009) described anorthoclase phenocrysts from trachytes erupted at
 506 Pantelleria with similar plagioclase composition cores, suggesting that they may have formed
 507 from benmoreitic magmas, trapped in lower, dense and viscous portions of the storage system by
 508 a trachytic ‘trap’ zone. The ‘filtering’ effects of density stratified peralkaline magma reservoirs
 509 have previously been cited as a mechanism for ‘Daly Gap’ formation at Aluto (Gleeson et al.,
 510 2017), as well as Gedemsa (Peccerillo et al., 2003) volcano in the MER. Careful examination of
 511 the Fentale welded tuff by Gibson (1974) has revealed that it was erupted from a
 512 compositionally- and therefore likely density-stratified storage region.

513 The best-fit RhyoliteMELTS models for Aluto (Gleeson et al., 2017), Kone, and Fentale
 514 suggest, in addition, that these compositions may be physically scarce, with fractionating
 515 magmas passing rapidly through the intermediate stages. The models show that SiO₂ does not
 516 vary linearly with temperature (**figure 8a**) or melt fraction (F) (**figure 8b**), which corresponds to
 517 the degree of crystallisation (1-F). Mushkin et al. (2002) presented an equation for estimating the
 518 rate of change of differentiation:

519

$$520 \quad \frac{\partial \text{SiO}_2}{\partial t} \propto \frac{\partial \text{SiO}_2}{\partial H} (T_m - T_0) V^{\frac{2}{3}} \quad (1)$$

521

522 , where $\frac{\partial \text{SiO}_2}{\partial t}$ is the rate of change of SiO₂, H is the released heat at each melt temperature (T_m)
 523 and V is the melt volume. The wall rock temperature (T_0) has been varied as it is not output from
 524 the RhyoliteMELTS models. The models predict that faster rates of differentiation occur
 525 between ~50 to ~65 wt% SiO₂ (**figure 8c**). This has been suggested as the result of separation of
 526 SiO₂-poor minerals over this narrow interval (Clague, 1978; Gleeson et al., 2017; Peccerillo et
 527 al., 2003). This rapid differentiation may aid preservation of the plagioclase feldspar cores
 528 observed at Aluto, Kone, and Fentale, with timescales too short for complete re-equilibration.
 529 The occurrence of the ‘Daly Gap’ is likely due to a combination of factors, including the
 530 predicted scarcity of intermediate compositions produced during fractionation, and the density
 531 stratification of zoned storage systems that may keep potentially crystal-rich zones of
 532 intermediate magmas locked away.

533

534 5.3 Heterogeneous crystal cargoes: evidence for entrainment of antecrysts

535 While the whole-rock and glass geochemistry displays clear trends related to fractional
 536 crystallisation, there is significant heterogeneity in the trace element composition of the feldspars
 537 (**figure 9**). The Ba concentrations in the rims of individual feldspars within a sample can vary
 538 greatly, reflected in the unsystematic divergence between whole-rock and glass measurements of
 539 feldspar compatible traces such as Ba (**figure 5c**). This suggests that a portion of the feldspars
 540 are antecrystic, particularly within the crystal-rich ignimbrite samples, where glomerocrystic
 541 clots of crystals, consistent with this interpretation, are prevalent. While phase equilibria will
 542 maintain alkali feldspar compositions at around Or 35±5% for evolved peralkaline melts (Bailey,
 543 1974; Bailey et al., 1974; Bailey & Schairer, 1964; Carmichael & MacKenzie, 1963; Nicholls &
 544 Carmichael, 1969; Thompson & MacKenzie, 1990), the trace element contents of the feldspars

545 are expected to vary as crystallisation continues owing to the relatively large changes in trace
 546 element concentrations in melts during crystallisation (and changing partitioning behaviour with
 547 temperature and melt composition). Therefore, detailed trace element analysis is needed in order
 548 to reveal the true complexity of feldspars in these systems.

549 Ba partitioning between feldspar and peralkaline silicate melt depends largely on
 550 temperature and melt composition (in particular peralkalinity) (Henderson & Pirozynski, 2012).
 551 It has been suggested that Ba feldspar-melt partition coefficients drop steeply with peralkalinity,
 552 despite the accompanying modest increases in SiO₂ and drop in temperatures (Henderson &
 553 Pirozynski, 2012; Mahood & Stimac, 1990). This is due to increasing melt SiO₂ content being
 554 accompanied by a decline in network-forming Al and an increase in Fe content, leading to Ba
 555 becoming very incompatible in feldspar crystals in highly evolved peralkaline melts. Here we
 556 have predicted melt Ba contents from the observed feldspar rim trace element geochemistry. Ba
 557 alkali feldspar-melt partition coefficients (D_{Ba}) are based on **equation 2** from the experimental
 558 work of Henderson and Pirozynski (2012):

$$559 \ln(D_{Ba}) = 37.8 - 0.06NKA - 0.037T \quad (2)$$

561 , where NKA is the glass peralkalinity (Na₂O + K₂O)/Al₂O₃, mol%), temperature was set at 765
 562 °C (Gleeson et al., 2017). **Figure 9** shows that in many cases the predicted melt Ba value is
 563 much higher than that of the observed, indicating that the feldspars are not in equilibrium with
 564 their carrier melt. As the partition coefficients calculated by this method are strongly dependent
 565 on melt peralkalinity it should be again be noted that several Kone samples may have low NKA
 566 due to Na loss (**supplementary 1**; White et al., 2003). Partition coefficients calculated for these
 567 samples may therefore be much higher than the true values and will produce lower predicted
 568 melt Ba concentrations. An adjusted value, based on the relationship between the FK/A and A.I.
 569 indicators of peralkalinity (White et al., 2003) has also been used in these calculations, producing
 570 more reasonable predicted melt Ba in these cases. Melt Ba contents based on the ‘effective’
 571 partition coefficients, observed in natural samples, of Mahood and Stimac (1990) are also
 572 indicated by the thick solid lines. The lower D_{Ba} of 1.2 is largely consistent with the relationship
 573 between the observed feldspar and melt Ba contents, however the higher D_{Ba} of 5.9 given by
 574 Mahood and Stimac (1990) again predicts much higher melt Ba contents based on the feldspar
 575 rims.
 576

577 Ba partitioning behaviour between alkali feldspars and melt, as constrained by Henderson
 578 and Pirozynski (2012), was also used to produce a simple fractional crystallisation model based
 579 on RhyoliteMELTS simulations (Gualda et al., 2012) of the liquid line of descent (shown in
 580 **figure 3 and 4**). Partition coefficients are calculated using **equation 2** for each major element
 581 melt composition produced by RhyoliteMELTS, which are then converted to bulk partition
 582 coefficients using the mineral assemblages output by RhyoliteMELTS, assuming negligible
 583 intake of Ba by phases other than feldspar. This bulk partition coefficient is then input into a
 584 fractional crystallisation equation:

$$585 \frac{c_i^l}{c_i^o} = (1 - X)^{D-1} \quad (3)$$

587

588 , where i is the element of interest, C^o is the original concentration in the parental liquid, taken
 589 from the Ba contents of the starting basalts input into RhyoliteMELTS (17-01-05 for Aluto,
 590 MER133A for Kone, F12 for Fentale), C^l is the concentration in the liquid, D is the solid-melt
 591 partition coefficient, F is the melt fraction, and X is the fraction of material crystallised.

592 The results of the modelling are shown in **figure 10**, along with the observations from the
 593 Aluto, Kone and Fentale samples, and the experimental glasses on which the Ba feldspar-melt
 594 partitioning behaviour is based (Henderson & Pirozynski, 2012) as well as some natural Ba data
 595 for pantellerite samples (Mahood & Stimac, 1990). The feldspar-melt partition coefficients for
 596 Ba (D_{Ba}), predicted by RhyoliteMELTS combined with the empirical Ba partitioning behaviour
 597 described by Henderson & Pirozynski (2012), extend only up to 0.5 for the evolved
 598 compositions investigated, quickly dropping again as the SiO_2 content, and consequently the
 599 peralkalinity, increases (**figure 10c and 10d**). These very low partition coefficients mean that the
 600 model predicts the Ba content of the melt to rise rapidly (**figure 10b**) and feldspar Ba contents to
 601 peak at only 1000 ppm (**figure 10a**). The Fentale model predicts much lower values for D_{Ba} , and
 602 consequently the feldspars too. However, it is likely that these model partition coefficients are
 603 too low, due to the overestimation of melt peralkalinity in RhyoliteMELTS. We believe that
 604 observations of Ba partitioning in the experimental glasses of Henderson & Pirozynski (2012)
 605 and the natural unzoned pantelleritic samples of Mahood and Stimac, (1990) produce more
 606 realistic estimates of partition coefficients (**figure 10**).

607 The natural data from the MER volcanoes show high and variable feldspar rim Ba
 608 concentrations (**figure 10a**), and melt Ba concentrations of 60 to 850 ppm (**figure 10b**), thereby
 609 yielding higher and more variable ‘apparent’ feldspar-melt partition coefficients, calculated
 610 using feldspar rim values and average melt compositions, than predicted. This is particularly
 611 notable in samples from eruptions associated with caldera-forming events (**figure 10c and 10d**).
 612 Mahood and Stimac (1990) produced *observed* partition coefficients for five pantellerites and
 613 trachytes from Pantelleria by averaging data from unzoned phenocrysts, the upper and lower
 614 values of the range they calculated are shown on **figure 10c and 10d**. The majority of ‘apparent’
 615 partition coefficients calculated for the MER volcanic samples fall within this range, and
 616 therefore so do the averaged observed partition coefficient for each sample. However, the spread
 617 of ‘apparent’ coefficients is large, producing large standard deviations, particularly for the
 618 caldera-forming samples which show can show a σ of up to 5.5 (**table 3**). Mahood and Stimac
 619 (1990) cite zoning as the likely cause of variability in literature values for feldspar-melt Ba
 620 partition coefficients, however this has been ruled out in this study by only using rims of crystals
 621 that appear themselves to be unzoned (**figure 7a and b**). It should also be noted that the data do
 622 not show a fall in the partition coefficients, predicted for increasingly evolved (**figure 10c**),
 623 increasingly peralkaline melts (**figure 10d**) (Henderson & Pirozynski, 2012; Mahood & Stimac,
 624 1990). However these studies were limited to rhyolites with <70 wt% SiO_2 , and may not be
 625 representative of the high silica rhyolites we present.

626 We interpret these data (shown in **figures 9 and 10**) to show that a portion of the Ba-rich
 627 feldspars, particularly within the caldera-forming ignimbrite deposits, are antecrysts, crystallised
 628 from a Ba-rich (more primitive) melt, before being entrained into a Ba-depleted (more evolved)
 629 melt. One interpretation of this observation is that these antecrysts, during the process of
 630 fractional crystallisation, were segregated from the melt and stored in a distinct region of the
 631 magma reservoir. This crystallisation and segregation of alkali feldspars would continually strip

632 the melt of compatible elements, such as Ba, sequestering them in the crystals. At some point
633 before or during eruption, the melt entrained these crystals, which may have been disaggregated
634 from a crystal-rich region of the reservoir. Textural evidence of mush disaggregation can be
635 observed in the prevalence of glomerocrystic clots of feldspars in the crystal-rich ignimbrites.
636 We propose a conceptual structure for the peralkaline magma reservoirs beneath Aluto and Kone
637 that is consistent with the evidence we present here (**figure 11**). The reservoir may contain
638 feldspar-rich ‘mush’ regions, with segregated residual liquids in the upper portions. This
639 structure is consistent with the hypothesis that the ‘Daly Gap’ may be caused by density filtering,
640 with less evolved magmas locked away in crystal-rich mushes (see section 5.2). Post-caldera
641 eruptions primarily tap the residual liquids, with relatively low fractions of antecrysts, whilst
642 more explosive, larger volume eruptions, associated with caldera-forming events, may excavate a
643 mush pile, erupting a cargo of more Ba-enriched crystals out of equilibrium with the carrier
644 liquid (**figure 9 and 10a**). The absence of notable trace element zoning in the antecrysts (**figure**
645 **7a and 7b**) suggests that conditions are not suitable for rim growth and/or the timescale between
646 crystal accumulation and eruption is short. Ba is a slow diffusing element (Cherniak, 2002)
647 which would require the timescales for equilibration to be long: equilibration of 100 micron thick
648 rims at 700 °C would require timescales of Ma (Cherniak, 2002). It may be that long-term
649 storage in a ‘mush region’ has resulted in the diffusive homogenisation of the crystals, removing
650 any zoning developed during growth in a continually evolving liquid, prior to incorporation into
651 their final carrier liquid. We speculate that this crystal scavenging may have taken place during
652 eruption, although the timing of it remains unconstrained.

653 High crystallinity ‘mush’ bodies have been inferred to exist in the crust beneath other
654 volcanoes in the EAR. Rooney et al. (2012) invoked a crystal-mush model to explain the
655 chemical heterogeneity of the crystal cargo at Chefe Donsa. Macdonald et al (2008) observed
656 cumulate feldspar-rich xenoliths enriched in Ba, Sr and Eu at peralkaline centres in the Kenyan
657 Rift, whilst the elevated Ba contents of some melts from the Olkaria Volcanic Complex, Kenyan
658 Rift, have been linked to resorption of remobilised alkali feldspars (Macdonald et al., 2012).
659 Marshall et al (2009) also observed disequilibrium features in phenocrysts that were tentatively
660 linked to crystal scavenging at Olkaria. At Menengai volcano, there is isotopic consistency
661 between phenocrysts that are out of equilibrium with their carrier melts in terms of trace
662 elements, indicating a common genetic source for the antecrysts (Macdonald et al., 1994).
663 Gibson (1974) also suggested that the differing geochemistry of pre- and post-caldera deposits at
664 Fentale volcano may even relate to the loss of ‘fugitive material’ during large caldera eruptions.
665 The data from this study supports this link, with lower Ba concentrations observed in the Fentale
666 post-caldera whole-rock, glass and feldspar analyses. The absence of this pattern at Kone may be
667 related to the volcanoes history of multiple caldera eruptions, where pre-Kone caldera samples
668 may also be viewed as post-Birenti caldera samples. The only non-caldera sample to contain
669 feldspars with significant Ba concentrations was the singular pre-Birenti obsidian investigated.

670

671 5.4 Timescales of crystal settling and compaction in a peralkaline magma reservoir

672 Segregation of liquids and crystals during protracted fractional crystallisation is an
673 important process in the evolution of Aluto, Kone, and Fentale peralkaline magmas. Our data
674 suggest that residual melts are stripped of compatible trace elements, such as Ba, which are
675 sequestered in feldspars in crystal mush piles (**figure 11**). Observations of crystal-poor
676 peralkaline rhyolites erupted between caldera-forming events requires the segregation of liquids

677 from crystals on timescales at least reflecting the inter-eruption periods. The efficiency of
678 settling and compaction may be aided by the relatively low viscosity of peralkaline melts: at 800
679 °C the Cuddia di Mida pantellerite viscosity lies between 5×10^3 and 5×10^4 Pa s for H₂O
680 concentrations of 2.5-4.9 wt% (Neave et al., 2012). This low melt viscosity promotes magma
681 differentiation and stratification through crystal settling; Stokes settling velocities of 10, 190 and
682 230 Ma^{-1} were reported for 1 mm grains of plagioclase, augite and olivine (Neave et al., 2012).

683 Here we calculate the timescales necessary for melt segregation in a peralkaline system
684 similar to Aluto following the method of Bachmann and Bergantz (2004) (for details of the
685 modelling see **supplementary 4-6**; Barnea & Mizrahi, 1973; Davis and Scriver, 1985;
686 Jackson et al., 2003; McKenzie, 1984; Rabinowicz et al., 2001; Shirley, 1986). A melt viscosity
687 of 10^2 Pa s was used for the peralkaline melt, based on the model of di Genova et al. (2013) for a
688 melt with 5 wt. % H₂O and a temperature of 765°C, values which are considered representative
689 for MER volcanics (Gleeson et al., 2017; Webster et al., 1993). We assume a density contrast
690 between melt and crystals of 170 kg/m^3 , based on the dominance of alkali feldspar (2550-2630
691 kg/m^3) and quartz (2650 kg/m^3), and a melt density of 2390 kg/m^3 (following Bottinga & Weill,
692 1970). All particles are assumed to be spherical and therefore these timescales are minima owing
693 to the decrease in settling velocity within a fluid with departure of a grain from a spherical shape
694 (Komar & Reimers, 1978). Porosity was set at 50% for compaction calculations based on
695 estimates of when a rigid crystal framework is formed for spherical particles (Vigneresse et al.,
696 1996); crystal fraction was set at 10% for hindered settling calculations based on the upper end
697 of phenocryst contents in post-caldera eruption deposits; see **supplementary 7 and 8** for the
698 effect of varying these parameters. Magma reservoir geometries were calculated assuming an
699 elliptical cylinder. The elliptical cross section had a long axis of 8 km and short axis of 5 km, in
700 line with the estimate of caldera size by Hutchison et al. (2015). There is considerable
701 uncertainty on the estimate of reservoir size. If the elliptical cross section used has 50% less area
702 then all estimates of compaction timescales will be an order of magnitude faster, whilst all
703 estimates of hindered settling will be two times slower (see **supplementary 9**). The model set-up
704 is shown in **supplementary 5**. Timescales of melt segregation for a metaluminous rhyolite melt
705 were modelled for comparison. Melt viscosity in this case was assumed to be 10^5 Pa s, assuming
706 a similar melt temperature and water content (Scaillet et al, 1998).

707 Mean eruption intervals at Aluto have been estimated at 300-400 years for post-caldera
708 pantellerites (**figure 12**; Fontijn et al., 2018). We calculated the timescales required to segregate
709 0.01 km^3 and 1 km^3 of melt, consistent with the range in eruptive volumes of crystal-poor post-
710 caldera eruptions at Aluto. For a mean grain size of 0.2 mm, it would take on the order of months
711 to tens of years to segregate 0.01 km^3 melt (**figure 12**), and tens of years to 10,000s of years to
712 segregate 1 km^3 melt from a crystalline mush, if we treat the magma reservoir as one coherent
713 body. The eruption intervals are typically greater than the upper limits required for melt
714 segregation suggested by the calculations, implying that there is sufficient time between
715 eruptions to extract enough melt for a post-caldera eruption of crystal-poor magma. It must be
716 stressed that this is a simple model, it may be that there are multiple regions of melt
717 accumulation in the reservoir, which would then decouple the eruption frequency from the time
718 scale needed to accumulate a particular volume of melt. Our results do highlight however, that
719 crystal-melt segregation is faster for peralkaline systems, with more than an order of magnitude
720 difference between the timescales versus a metaluminous system (**figure 12**).

721

722 5.5 Pre-eruptive Magma Storage Conditions

723 The pre-eruptive melt temperature of the Kone basaltic scoria was estimated using the
724 clinopyroxene-liquid thermobarometer of Neave and Putirka (2017) (see **supplementary 10 and**
725 **11** for further details). Clinopyroxene-melt equilibrium was last achieved at a temperature of
726 $1150\text{-}1170 \pm 60$ °C and pressures of $420\text{-}575 \pm 140$ MPa, equivalent to a depth of $15\text{-}21 \pm 5$ km
727 assuming an average crustal density of 2800 gm^{-3} (Wilks et al., 2017). The Fe-Mg partitioning
728 relationship between clinopyroxene and melt was used to select appropriate crystal rims for
729 analysis. Observed partition coefficients (D_{Fe-Mg}) between the pyroxenes melt all lay within
730 error of the 0.27 equilibrium value (Putirka, 2008).

731 The pre-eruptive temperature of the pantellerites at Aluto was estimated by Gleeson et al.
732 (2017) at $718\text{-}765 \pm 23$ °C using an alkali feldspar thermometer (Putirka, 2008) and assuming an
733 equilibration pressure of 150 MPa based on estimates using RhyoliteMELTS models (Gualda et
734 al., 2012). These pressures convert to depths of 5.4 ± 1 km assuming an average crustal density
735 of 2800 gm^{-3} (Wilks et al., 2017). Experimental studies have shown that the phase assemblage of
736 alkali feldspar, clinopyroxene, aenigmatite, and ilmenite is stable at 1.0-1.5 kbar at near H₂O-
737 saturated conditions and temperatures of 680-725 °C (di Carlo et al., 2010), largely consistent
738 with the Aluto observations. Further North, in the Afar region, Field et al (2012) analysed melt
739 inclusions from the peralkaline Dabbahu volcano, finding volatile saturation pressures in the
740 range of 43-207 MPa, also consistent with shallow magma storage, at ~1-5 km depth in the crust.

741 However it should be noted, concerning temperature estimates, that we have highlighted
742 complex crystal cargoes in pantellerite samples at Aluto, containing numerous alkali feldspars
743 that are likely to be out of equilibrium with their host melts. These can often be difficult to
744 identify based on petrographic observations and major-element analysis alone. If temperatures
745 are higher than estimated by Gleeson et al. (2017), calculated feldspar-melt Ba partition
746 coefficients will be lower, and thus predicted melt Ba based on feldspar rim compositions will be
747 higher. If lower than estimated, partition coefficients will be higher and predicted melt Ba
748 contents lower.

749

750 6 Implications of our study for geophysical imaging of peralkaline magma reservoirs

751 Whilst whole-rock and glass compositions of erupted products from Aluto, Kone, and
752 Fentale reflect prolonged fractional crystallisation (**figures 3-5**), trace element heterogeneity in
753 the crystal cargoes (**figure 9 and 10a**) is indicative of more complex processing including
754 mixing and crystal scavenging, perhaps from a mush-dominated magma storage system. In
755 support of a mush-dominated system, low-viscosity peralkaline liquids allow for efficient
756 crystal-melt segregation, (**figure 12**) building mush piles where intermediate composition melts
757 are locked away, and compatible elements, such as Ba, are sequestered. We suggest that crystal-
758 rich ignimbrites, associated with caldera-forming events, may be able to scavenge Ba-enriched
759 antecrysts from this region (**figure 11**). Post-caldera eruptions primarily tap residual melt,
760 segregated in small melt lenses in the upper portions of the reservoir, with a much lower fraction
761 of scavenged antecrysts.

762 Magnetotelluric surveys, used for inferring the Earth's subsurface electrical conductivity,
763 have been conducted at several sites along the EARS (Desissa et al., 2013; Hübner et al., 2018;
764 Johnson et al., 2015; Samrock et al., 2015 Whaler & Hautot, 2006). Resistivity is sensitive to

765 fluid content, allowing the method to identify the presence of partial melt beneath volcanoes
766 (Desissa et al., 2013; Johnson et al., 2015). However, the electrical conductivity of magmatic
767 reservoirs is dependent on the state of the magma itself, in terms of melt volatile abundance,
768 temperature, composition, and crystal content (Gaillard & Iacono Marziano, 2005). The
769 electrical conductivity of silicate liquids varies within a range of 10^{-2} - 10^1 ohm m^{-1} (Gaillard,
770 2004; Tyburczy & Waff, 1985; Waff & Weill, 1975), whilst the conductivity of crystals can be
771 in the range of 10^{-10} - 10^{-3} ohm m^{-1} (Huebner & Dillenburg, 1995), making them insulators. A
772 highly crystalline mush, with a low melt fraction, may appear as a resistive structure (Hübert et
773 al., 2018). Indeed, despite the petrological estimates for shallow magma storage at Aluto
774 (Gleeson et al., 2017), as described above, magnetotelluric methods have not identified an area
775 of increased electrical conductivity in the crust (Hübert et al., 2018; Samrock et al., 2015) that
776 might indicate the presence of partial melt (e.g., Pous et al., 1999; Hoffman-Rothe et al., 2011;
777 Schilling & Partzsch, 2001). At shallow depths a conductive clay cap to the hydrothermal system
778 is proposed, whilst at greater depths the crust appears increasingly resistive (Hübert et al., 2018;
779 Samrock et al., 2015).

780 Small lenses of residual melt in the upper part of the system, which we hypothesise feed
781 the crystal-poor post-caldera eruptions, accumulate over short timescales (10^{-1} - 10^1 years). Small-
782 volume liquid lenses may be difficult to capture and resolve using conductivity surveys due to
783 the inherently low spatial resolution of the technique. The ephemeral nature of these liquid lenses
784 poses new challenges when imaging and monitoring peralkaline magmatic-volcanic systems,
785 with a need to better understand the limits of detection and the time-dependent evolution of
786 magmatic storage regions. The presence of a conductive anomaly at Boset-Bericha volcano
787 (Whaler & Hautot, 2006), for example, may reflect the time-sensitive capture of short-lived melt-
788 lens, although it could also indicate the presence of a longer-lived more melt-rich, interconnected
789 system. The scenarios at both Aluto and Boset-Bericha are in stark contrast to electrical
790 resistivity surveys carried out further North in the Afar region. Here large regions of low
791 resistivity have been imaged reaching down to 35 km depth, interpreted as long-lived reservoirs
792 containing ~13% melt fraction and extending down into the mantle (Desissa et al., 2013).

793 Other geophysical data from Aluto are consistent with a magma reservoir system
794 extending to depths of 9 km and deeper. A local network of 12 seismometers was deployed at
795 Aluto between 2012 and 2014, detecting more than 2000 earthquakes in a 24-month period
796 (Wilks et al., 2017). A shallow zone (at 0-2 km) of high seismicity and high b-values (a
797 parameter describing the relative abundance of large to small magnitude events) likely
798 corresponds to the active hydrothermal system, while deeper events (2-9 km) reflect high strain
799 rates where magmatic fluids cause elastic deformation (Wilks et al., 2017). At depths greater
800 than 9 km the crust appears largely aseismic, interpreted as an area of underlying ductile
801 magmatic mush (Wilks et al., 2017). These interpretations are largely consistent with those
802 arising from InSAR observations of deformation at Aluto. A period of inflation in 2008 is best
803 explained by a deformation source at $\sim 5.1 \pm 0.5$ km depth, thought to reflect fluid injection into
804 the roof zone of a magma storage region (Hutchison et al., 2016a). A subsequent period of long-
805 term subsidence was interpreted as magmatic degassing and depressurisation of the hydrothermal
806 system (Hutchison et al., 2016a). Mahatsente et al. (1999) additionally located a positive gravity
807 anomaly within the shallow crust beneath Aluto during a regional survey. This could be
808 consistent with the presence of crystalline magmatic intrusions, and may provide evidence for
809 density filtering of intermediate magmas forming a 'Daly Gap' at Aluto (see section 5.2). Mattia

810 et al. (2007) suggested that trapped high-density intermediate magmas at Pantelleria may
811 contribute to the positive gravity anomalies observed there.

812 InSAR observations of the Afar region have also been used to suggest shallow magmatic
813 storage beneath volcanoes such as Dabbahu (Field et al., 2012; Grandin et al., 2010; Wright et
814 al., 2006). Here a broad area of uplift, ~20 km in diameter, was shown to be consistent with a
815 modelled scenario of stacked sills at 1-6 km depth. Seismic data obtained during the same period
816 of unrest indicated similar depths of storage (Ayele et al., 2007; Ebinger et al., 2008; Field et al.,
817 2012). Whilst silicic centres in the Afar region, such as Dabbahu, may appear similar to those of
818 the MER in terms of peralkaline compositions and shallow storage, contrasting crustal electrical
819 resistivity again highlights key differences. In this more mature Afar rift, large volumes of partial
820 melt are stored throughout the crust (Desissa et al., 2013), magma flux to the surface appears to
821 be greater (Hutchison et al., 2018) and eruptions are more frequent. At least five eruptions have
822 occurred in Afar during the period of modern remote sensing (e.g., Allard et al., 1979; Ayele et
823 al., 2007; Ayele et al., 2009; Ferguson et al., 2010; Grandin et al., 2009; Wright et al., 2006;
824 Yirgu et al., 2006) whereas none have occurred in the MER. Silicic magmatic plumbing in the
825 Afar region is also clearly linked to the rifting cycle. For example, Wright et al. (2006) showed
826 that much of the melt supplied to a major dyking episode in 2005 was sourced from shallow
827 chambers beneath the Dabbahu and Gabho volcanoes. In Afar magma storage reservoirs appear
828 to be more connected and, potentially, laterally extensive (Biggs et al., 2016; Ebmeier et al.,
829 2018; Xu et al., 2017) compared to the MER, where we hypothesise small portions of melt stored
830 in poorly connected, ephemeral lenses.

831 **7 Conclusions**

832 While whole-rock and glass compositions are modelled effectively by fractional
833 crystallisation, this simple model cannot explain the trace element (Ba) heterogeneity observed
834 in the crystal cargoes from eruptive products at Aluto, Kone, and Fentale volcanoes. Many of the
835 feldspars, particularly in samples from caldera-forming eruptions, are antecrysts, crystallised
836 from a Ba-enriched (more primitive) melt, before being segregated during the process of
837 fractional crystallization, and later entrained in Ba-depleted (more evolved) residual liquids. We
838 propose that these antecrysts are sourced from a crystal-rich region of the magma reservoir
839 (perhaps a ‘mush’) that is excavated during the largest eruptions, creating crystal-rich trachytes
840 and rhyolites typical of caldera-forming eruptions.

841 The low-viscosity nature of peralkaline rhyolitic liquids causes crystal-melt segregation
842 to occur on faster timescales than for metaluminous rhyolites (which are more viscous).
843 Separated crystals sequester compatible elements such as Ba, whilst residual melts continue to
844 evolve, likely going on to feed post-caldera eruptions. The timescales necessary for the
845 segregation of enough residual, eruptible melt to feed a crystal-poor post-caldera eruption (0.01-
846 1 km³) are short (10¹-10⁴ years). These isolated melt lenses may be small and ephemeral, perhaps
847 making them difficult to resolve using geophysical techniques (seismic tomography, electrical
848 conductivity). The interpretation that peralkaline systems may spend portions of their life cycle
849 dominated by crystalline mushes helps reconcile contrasting geophysical data for Aluto.

850 Our study highlights the absence of experimental data for Ba partitioning behavior in
851 silica-rich peralkaline melts; and the deficiencies in the RhyoliteMELTS model at reproducing
852 peralkalinity for the rhyolitic end of the magma series. This causes partitioning models, which
853 depend on peralkalinity, to consistently underestimate feldspar-melt partition coefficients for Ba

854 and feldspar Ba contents. A previous study suggested that Ba feldspar-melt partition coefficients
855 drop steeply with peralkalinity despite accompanying modest increases in SiO₂ and drop in
856 temperatures (Mahood & Stimac, 1990); however, this study, and the experimental data of
857 Henderson and Pierozynski (2012), was limited to rhyolites with <70 wt% SiO₂. Petrological
858 experiments on more evolved peralkaline magmas are needed to improve our understanding of
859 Ba partitioning in peralkaline rhyolitic magmas.

860 **Acknowledgments**

861 We acknowledge the expertise and assistance provided by colleagues from Addis Ababa
862 University and the kind permission of national and regional authorities during fieldwork and
863 sample collection. We thank John White and Tyrone Rooney and two anonymous reviewers for
864 their helpful reviews and encouragement. Data from this study can be found in the
865 supplementary files. This project is funded by the Natural Environment Research Council grant
866 NE/L013932/1 (RiftVolc).

867 **References**

- 868 Abebe, B., Acocella, V., Korme, T. & Ayalew, D. (2007). Quaternary Faulting and Volcanism in
869 the Main Ethiopian Rift. *Journal of African Earth Sciences* 48, 115–124.
- 870 Acocella, V., Korme, T., Salvini, F. & Funicello, R. (2002). Elliptic calderas in the Ethiopian
871 Rift: control of pre-existing structures. *Journal of Volcanology and Geothermal Research* 119,
872 189–203.
- 873 Agostini, A., Bonini, M., Corti, G., Sani, F. & Mazzarini, F. (2011). Fault Architecture in the
874 Main Ethiopian Rift and Comparison With Experimental Models: Implications for Rift Evolution
875 and Nubia–Somalia Kinematics. *Earth and Planetary Science Letters* 301(3), 479–492.
- 876 Ayele, A., Jacques, E., Kassim, M., Kidane, T., Omar, A., Tait, S., Nercessian, A., et al (2007).
877 The volcano-seismic crisis in Afar, Ethiopia starting September 2005. *Earth and Planetary
878 Science Letters* 255 (1-2), 177–187.
- 879 Ayele, A., Keir, D., Ebinger, C., Wright, T.J., Stuart, G.W., Buck, W.R., Jacques, E., et al.
880 (2009). September 2005 mega-dike emplacement in the Manda-Harraro nascent oceanic rift
881 (Afar depression). *Geophysical Research Letters* 36(20).
- 882 Bachmann, O. & Bergantz, G. (2004). On the Origin of Crystal poor Rhyolites: Extracted from
883 Batholithic Crystal Mushes. *Journal of Petrology* 45(8), 1565–1582.
- 884 Bachmann, O. & Bergantz, G. (2008). The Magma Reservoirs That Feed Supereruptions.
885 *Elements* 4(1), 17–21.
- 886 Bachmann, O., Dungan, M. & Lipman, P. (2002). The Fish Canyon Magma Body, San Juan
887 Volcanic Field, Colorado: Rejuvenation and Eruption of an Upper-Crustal Batholith. *Journal of
888 Petrology* 43(8), 1469–1503.
- 889 Bailey, D. (1974). Experimental Petrology Relating to Oversaturated Peralkaline Volcanics: A
890 Review. *Bulliten of Volcanology* 38, 635–652.
- 891 Bailey, D., Cooper, J. & Knight, J. (1974). Anhydrous Melting and Crystallisation of Peralkaline
892 Obsidians. *Bulliten of Volcanology* 38, 653–665.

- 893 Bailey, D. & Schairer, J. (1964). Feldspar-Liquid Equilibria In Peralkaline Liquids - The
894 Orthoclase Effect. *American Journal of Science* 262, 1198–1206.
- 895 Barberi, F., Ferrara, G., Santacroce, R., Treuil, M. & Varet, J. (1975). A Transitional Basalt-
896 Pantellerite Sequence of Fractional Crystallisation, the Boina Centre (Afar Rift, Ethiopia).
897 *Journal of Petrology* 16(1), 22–56.
- 898 Barberi, F., Santacroce, R. & Varet, J. (1974). Silicic Peralkaline Volcanic Rocks of the Afar
899 Depression (Ethiopia). *Bulliten of Volcanology* 38(2), 755–790.
- 900 Barclay, J., Carroll, M. R., Houghton, B. F., & Wilson, C. J. N. (1996). Pre-Eruptive Volatile
901 Content and Degassing History of an Evolving Peralkaline Volcano. *Journal of Volcanology and*
902 *Geothermal Research* 74, 75–87.
- 903 Barnea, E. & Mizrahi, J. (1973). A Generalized Approach to the Fluid Dynamics of Particulate
904 Systems. Part I. General Correlation for Fluidization and Sedimentation in Solid Multiparticulate
905 Systems. *Chemical Engineering Journal* 5, 171–189.
- 906 Beard, J. & Lofgren, G. (1991) Dehydration Melting and Water-Saturated Melting of Basaltic
907 and Andesitic Greenstones and Amphibolites at 1, 3, and 6.9 Kb. *Journal of Petrology* 32(2),
908 365–401.
- 909 Biggs, J., Keir, D. & Lewi, E. (2011). Pulses of Deformation Reveal Frequently Recurring
910 Shallow Magmatic Activity beneath the Main Ethiopian Rift. *Geochemistry, Geophysics,*
911 *Geosystems* 12(9), 1–11.
- 912 Biggs, J., Robertson, E. & Cashman, K. (2016). The lateral extent of volcanic interactions during
913 unrest and eruption. *Nature Geoscience* 9, 308–311.
- 914 Bilham, R., Bendick, R., Larson, K., Mohr, P., Braun, J., Tesfaye, S. & Asfaw, L. (1999).
915 Secular and tidal strain across the main Ethiopian rift. *Geophysical Research Letters* 26(18),
916 2789–2792.
- 917 Blake, S. & Ivey, G. (1986). Magma-Mixing and the Dynamics of Withdrawal from Stratified
918 Reservoirs. *Journal of Volcanology and Geothermal Research* 27(1-2), 153–178.
- 919 Boccaletti, M., Getaneh, A., Mazzuoli, R., Tortorici, L. & Trua, T. (1995). Chemical Variations
920 in a Bimodal Magma System: The Plio-Quaternary Volcanism in the Dera Nazret Area (Main
921 Ethiopian Rift, Ethiopia). *Africa Geoscience Review* 2(1), 37–60.
- 922 Bonini, M., Corti, G., Innocenti, F., Manettie, P., Mazzarini, F., Abebe, T. & Pecskey, Z.
923 (2005). Evolution of the Main Ethiopian Rift in the Frame of Afar and Kenya Rifts Propagation.
924 *Tectonics* 24, 1–21.
- 925 Bottinga, Y. & Weill, D. (1970). Densities of Liquid Silicate Systems Calculated from Partial
926 Molar Volumes of Oxide Components. *American Journal of Science* 269, 169–182.
- 927 Carmichael, I. & MacKenzie, W. (1963). Feldspar-Liquid Equilibria in Pantellerites: An
928 Experimental Study. *American Journal of Science* 261, 382–396.
- 929 Cashman, K.V. & Giordano, G. (2014). Calderas and magma reservoirs. *Journal of Volcanology*
930 *and Geothermal Research* 288, 28–45.
- 931 Cashman, K.V. & Sparks, R.S.J. (2013). How volcanoes work: A 25 year perspective.
932 *Geological Society of America Bulletin* 125(5-6), 664–690.

- 933 Cashman, K., Sparks, R., & Blundy, J. (2017). Vertically Extensive and Unstable Magmatic
934 Systems: A Unified View of Igneous Processes. *Science* 355(6331), eaag3055.
- 935 Chayes, F. (1963). Relative abundance of intermediate members of the oceanic basalt-trachyte
936 association. *Journal of Geophysical Research* 68(5), 1519–1534.
- 937 Chayes, F. (1977). The oceanic basalt-trachyte relation in general and in the Canary Islands.
938 *American Mineralogist* 62, 666–671.
- 939 Cherniak, D. J. (2002). Ba diffusion in feldspar. *Geochim Cosmochim Acta* 66(9), 1641–1650
- 940 Chu, R., Helmberger, D., Sun, D., Jackson, J. & Zhu, L. (2010). Mushy Magma beneath
941 Yellowstone. *Geophysical Research Letters* 37, 1–5.
- 942 Clague, D. (1987). Hawaiian xenolith populations, magma supply rates, and development of
943 magma chambers. *Bulletin of Volcanology* 49(4), 577–587.
- 944 Cole, J. (1969). Gariboldi Volcanic Complex, Ethiopia. *Bulliten of Volcanology* 33, 566–578.
- 945 Cooper, K. & Kent, A. (2014). Rapid Remobilization of Magmatic Crystals Kept in Cold
946 Storage. *Nature* 506(7489), 480–483.
- 947 Corti, G. (2008). Control of rift obliquity on the evolution and segmentation of the main
948 Ethiopian rift. *Nature Letters* 1, 258–262.
- 949 Corti, G. (2009). Continental Rift Evolution: From Rift Initiation to Incipient Break-up in the
950 Main Ethiopian Rift, East Africa. *Earth Science Reviews* 96, 1–53.
- 951 Davis, R. & Scrivos, A. (1985). Sedimentation of Noncolloidal Particles at Low Reynolds
952 Numbers. *Annual Reviews in Fluid Mechanics* 17(1), 91–118.
- 953 de Silva, S., Salas, G. & Schubring, S. (2008). Triggering Explosive Eruptions—The Case for
954 Silicic Magma Recharge at Huaynaputina, Southern Peru. *Geology* 36(5), 387–390.
- 955 Desissa, M., Johnson, N. E., Whaler, K. A., Hautot, S., Fisseha, S. & Dawes, G. J. K. (2013). A
956 mantle magma reservoir beneath an incipient mid-ocean ridge in Afar, Ethiopia. *Nature*
957 *geoscience*, 6(10), 861.
- 958 di Carlo, I., Rotolo, S., Scaillet, B., Buccheri, V. & Pichavant, M. (2010). Phase Equilibrium
959 Constraints on Pre-Eruptive Conditions of Recent Felsic Explosive Volcanism at Pantelleria
960 Island, Italy. *Journal of Petrology* 51(11), 2245–2276.
- 961 di Genova, D., Romano, C., Hess, K., Vona, A., Poe, B., Giordano, D., Dingwell, D., et al.
962 (2013). The Rheology of Peralkaline Rhyolites from Pantelleria Island. *Journal of Volcanology*
963 *and Geothermal Research* 249, 201–216.
- 964 Ebinger, C. J. (2005). Continental Break-Up: The East African Perspective. *Astronomy &*
965 *Geophysics* 46(2), 2–16.
- 966 Ebinger, C., Keir, D., Ayele, A., Calais, E., Wright, T.J., Belachew, M., Hammond, J.O., et al.
967 (2008). Capturing magma intrusion and faulting processes during continental rupture: seismicity
968 of the Dabbahu (Afar) rift. *Geophysical Journal International* 174, 1138–1152.
- 969 Ebmeier, S.K., Andrews, B.J., Araya, M.C., Arnold, D.W.D., Biggs, J., Cooper, C., Cottrell, E.,
970 et al. (2018). Synthesis of global satellite observations of magmatic and volcanic deformation:

- 971 implications for volcano monitoring & the lateral extent of magmatic domains. *Journal of*
972 *Applied Volcanology* 7(1), 2.
- 973 Ferguson, D.J., Barnie, T.D., Pyle, D.M., Oppenheimer, C., Yirgu, G., Lewi, E., Kidane, T.,
974 Carn, S. & Hamling, I. (2010). Recent rift-related volcanism in Afar, Ethiopia. *Earth and*
975 *Planetary Science Letters* 292 (3), 409–418.
- 976 Field, L., Blundy, J., Brooker, R.A., Wright, T.J. & Yirgu, G. (2012). Magma storage conditions
977 beneath Dabbahu Volcano (Ethiopia) constrained by petrology, seismicity and satellite geodesy.
978 *Bulletin of Volcanology* 74(5), 981–1004.
- 979 Fontijn, K., Elburg, M. A., Nikogosian, I. K., van Bergen, M. J., & Ernst, G. G. (2013).
980 Petrology and geochemistry of Late Holocene felsic magmas from Rungwe volcano (Tanzania),
981 with implications for trachytic Rungwe Pumice eruption dynamics. *Lithos*, 177, 34-53.
- 982 Fontijn, K., McNamara, K., Tadesse, A.Z., Pyle, D.M., Dessalegn, F., Hutchison, W., Mather,
983 T.A, et al. (2018). Contrasting styles of post-caldera volcanism along the Main Ethiopian Rift:
984 Implications for contemporary volcanic hazards. *Journal of Volcanology and Geothermal*
985 *Research* 356, 90-113.
- 986 Furman, T. (2006). Geochemistry of East African Rift basalts: An overview. *Journal of African*
987 *Earth Sciences* 48, 147–160.
- 988 Gaillard, F. (2004). Laboratory Measurements of Electrical Conductivity of Hydrous and Dry
989 Silicic Melts under Pressure. *Earth and Planetary Science Letters* 218(1-2), 215–228.
- 990 Gaillard, F. & Iacono Marziano, G. (2005). Electrical Conductivity of Magma in the Course of
991 Crystallisation Controlled by Their Residual Liquid Composition. *Journal of Geophysical*
992 *Research: Solid Earth* 110(B6), 1–12.
- 993 Garland, F., Hawkesworth, C. & Mantovani, M. (1995). Description and Petrogenesis of the
994 Paranà Rhyolites. *Journal of Petrology* 36(5), 1193–1227.
- 995 Gasparon, M., Innocenti, F., Manettie, P., Peccerillo, A. & Tsegaye, A. (1993). Genesis of the
996 Pliocene to Recent Bimodal Mafic-Felsic Volcanism in the Debre Zeyt Area, Central Ethiopia:
997 Volcanological and Geochemical Constraints. *Journal of African Earth Sciences* 17(2), 145–165.
- 998 Gibson, I.L.(1967). Preliminary Account of the Volcanic Geology of Fantale, Shoa. *Bulletin of*
999 *the Geophysical Observatory* 10, 59–67.
- 1000 Gibson, I. (1969). The Structure and Volcanic Geology of and Axial Portion of the Main
1001 Ethiopian Rift. *Tectonophysics* 8, 561–565.
- 1002 Gibson, I. (1970). A Pantelleritic Welded Ash-Flow Tuff fl'om the Ethiopian Rift Valley.
1003 *Contributions to Mineralogy and Petrology* 28, 89–111.
- 1004 Gibson, I.L. (1974). A review of the geology, petrology and geochemistry of the Volcano
1005 Fantale. *Bulletin of Volcanology* 38(2), 791–802.
- 1006 Giordano, F., D'Antonio, M., Civetta, L., Tonarini, S., Orsi, G., Ayalew, D., Yirgu, G., et al.
1007 (2014). Genesis and Evolution of Mafic and Felsic Magmas at Quaternary Volcanoes within the
1008 Main Ethiopian Rift: Insights from Gedemsa and Fanta 'Ale Complexes. *Lithos* 188, 130–144.

- 1009 Gleeson, M., Stock, M., Pyle, D., Mather, T., Hutchison, W., Yirgu, G. & Wade, J. (2017).
1010 Constraining Magma Storage Conditions at a Restless Volcano in the Main Ethiopian Rift Using
1011 Phase Equilibria Models. *Journal of Volcanology and Geothermal Research* 337, 44–61.
- 1012 Grandin, R., Socquet, A., Doin, M.P., Jacques, E., de Chabalier, J.B. & King, G.C.P. (2010).
1013 Transient rift opening in response to multiple dike injections in the Manda Hararo rift (Afar,
1014 Ethiopia) imaged by time-dependent elastic inversion of interferometric synthetic aperture radar
1015 data. *Journal of Geophysical Research* 115, B09403.
- 1016 Gualda, G., Ghiorso, M., Lemons, R. & Carley, T. (2012). Rhyolite-MELTS: A Modified
1017 Calibration of MELTS Optimized for Silica-Rich, Fluid-Bearing Magmatic Systems. *Journal of*
1018 *Petrology* 53, 875–890.
- 1019 Harris, 1844. The Highlands of Aethiopia, 2nd ed. Longman, Brown, Green and Longmans,
1020 London.
- 1021 Hay, E. & Wendlandt, R. (1995). The Origin of Kenya Rift Plateau-Type Phonolites: Results of
1022 High-Pressure/High-Temperature Experiments in the System Phonolite–H₂O and Phonolite–
1023 H₂O–CO₂. *Journal of Geophysical Research* 100, 401–410.
- 1024 Henderson, C., & Pirozynski, W. (2012). An Experimental Study of Sr, Ba and Rb Partitioning
1025 between Alkali Feldspar and Silicate Liquid in the System Nepheline-Kalsilite-Quartz at 0.1 GPa
1026 P(H₂O): A Revisitation and Reassessment. *Mineralogical Magazine* 76(1), 157–190.
- 1027 Hoffmann-Rothe, A., Ritter, O. & Haak, V. (2001). Magnetotelluric and Geomagnetic Modeling
1028 Reveals Zones of Very High Electrical Conductivity in the Upper Crust of Central Java. *Physics*
1029 *of the Earth and Planetary Interiors* 124, 131–151.
- 1030 Hübner, J., Whaler, K. & Fisseha, S. (2018). The Electrical Structure of the Central Main
1031 Ethiopian Rift as Imaged by Magnetotellurics - Implications for Magma Storage and Pathways.
1032 *Journal of Geophysical Research: Solid Earth* 123(7), 6019–6032.
- 1033 Huebner, J. & Dillenburg, R. (1995). Impedance Spectra of Hot, Dry Silicate Minerals and
1034 Rocks: Qualitative Interpretation of Spectra. *American Mineralogist* 80, 46–64.
- 1035 Humphreys, M., Blundy, J. & Sparks, S. (2008). Shallow-Level Decompression Crystallisation
1036 and Deep Magma Supply at Shiveluch Volcano. *Contributions to Mineralogy and Petrology*
1037 155(1), 45–61.
- 1038 Hutchison, W., Biggs, J., Mather, T., Pyle, D., Lewi, E., Yirgu, G., Caliro, S., et al. (2016a).
1039 Causes of Unrest at Silicic Calderas in the East African Rift: New Constraints from InSAR and
1040 Soil-Gas Chemistry at Aluto Volcano, Ethiopia. *Geochemistry, Geophysics, Geosystems* 17,
1041 3008–3030.
- 1042 Hutchison, W., Fusillo, R., Pyle, D., Mather, T., Blundy, J., Biggs, J., Yirgu, G., et al. (2016b) A
1043 Pulse of Mid-Pleistocene Rift Volcanism in Ethiopia at the Dawn of Modern Humans. *Nature*
1044 *Communications* 7, 13192.
- 1045 Hutchison, W., Mather, T., Pyle, D., Biggs, J. & Yirgu, G. (2015). Structural Controls on Fluid
1046 Pathways in an Active Rift System: A Case Study of the Aluto Volcanic Complex. *Geosphere*
1047 11(3), 1–21.
- 1048 Hutchison, W., Mather, T., Pyle, D., Boyce, A., Gleeson, M., Yirgu, G., Blundy, J., et al. (2018).
1049 The Evolution of Magma during Continental Rifting: New Constraints from the Isotopic and

- 1050 Trace Element Signatures of Silicic Magmas from Ethiopian Volcanoes. *Earth and Planetary*
1051 *Science Letters* 489, 203–218.
- 1052 Hutchison, W., Pyle, D., Mather, T., Yirgu, G., Biggs, J., Cohen, B., Barford, D., et al. (2016c).
1053 The Eruptive History and Magmatic Evolution of Aluto Volcano: New Insights into Silicic
1054 Peralkaline Volcanism in the Ethiopian Rift. *Journal of Volcanology and Geothermal Research*
1055 328, 9–33.
- 1056 Irvine, T. & Baragar, W. (1971). A Guide to the Chemical Classification of the Common
1057 Volcanic Rocks. *Canadian Journal of Earth Sciences* 8(5), 523–548.
- 1058 Jackson, M., Cheadle, M. & Atherton, M. (2003). Quantitative Modelling of Granitic Melt
1059 Generation and Segregation in the Continental Crust. *Journal of Geophysical Research* 108,
1060 2332.
- 1061 Johnson, N. E., Whaler, K. A., Hautot, S., Fisseha, S., Desissa, M., & Dawes, G. J. K. (2015).
1062 Magma imaged magnetotellurically beneath an active and an inactive magmatic segment in Afar,
1063 Ethiopia. *Geological Society, London, Special Publications*, 420, SP420-11.
- 1064 Keir, D., Bastow, I., Corti, G., Mazzarini, F. & Rooney, T. (2015). The Origin of Along-Rift
1065 Variations in Faulting and Magmatism in the Ethiopian Rift. *Tectonics* 34, 464–477.
- 1066 Keir, D., Ebinger, C., Stuart, G., Daly, E. & Ayele, A. (2006). Strain Accommodation by
1067 Magmatism and Faulting as Rifting Proceeds to Breakup: Seismicity of the Northern Ethiopian
1068 Rift. *Journal of Geophysical Research: Solid Earth* 111(B5).
- 1069 Kidane, T., Otofujii, Y., Komatsu, Y., Shibasaki, H. & Rowland, J. (2009). Paleomagnetism of
1070 the Fentale-magmatic segment, main Ethiopian Rift: New evidence for counterclockwise block
1071 rotation linked to transtensional deformation. *Physics of the Earth and Planetary Interiors* 176,
1072 109–123.
- 1073 Komar P.D., Reimers C.E. (1978). Grain shape effects on settling rates. *The Journal of Geology*
1074 86, 2, 193-209.
- 1075 Lanzo, G., Landi, P. & Rotolo, S. (2013). Volatiles in Pantellerite Magmas: A Case Study of the
1076 Green Tuff Plinian Eruption (Island of Pantelleria, Italy). *Journal of Volcanology and*
1077 *Geothermal Research* 262, 153–163.
- 1078 LeBas, M. J., Lemaitre, R.W., Streckeisen, A. & Zanettin, B. (1986). A Chemical Classification
1079 of Volcanic-Rocks Based on the Total Alkali Silica Diagram. *Journal of Petrology* 27(3), 745-
1080 750.
- 1081 Lowenstern, J., Clynne, M. & Bullen, T. (1997). Comagmatic A-Type Granophyre and Rhyolite
1082 from the Alid Volcanic Center, Eritrea, Northeast Africa. *Journal of Petrology* 38(12) 1707–
1083 1721.
- 1084 Macdonald, R. (1974) Nomenclature and Petrochemistry of the Peralkaline Oversaturated
1085 Extrusive Rocks. *Bulliten of Volcanology* 38, 498–505.
- 1086 Macdonald, R. (2012) Evolution of Peralkaline Silicic Complexes: Lessons from the Extrusive
1087 Rocks. *Lithos* 152, 11–22.

- 1088 Macdonald, R., Baginski, B., Leat, P., White, J. & Dzierzanowski, P. (2011). Mineral Stability in
1089 Peralkaline Silicic Rocks: Information from Trachytes of the Menengai Volcano, Kenya. *Lithos*
1090 *125*, 553–568.
- 1091 Macdonald, R., Baginski, B., Ronga, F., Dzierzanowski, P., Lustrino, M., Marzoli, A. &
1092 Melluso, L. (2012). Evidence for Extreme Fractionation of Peralkaline Silicic Magmas, the
1093 Boseti Volcanic Complex, Main Ethiopian Rift. *Miner Petrol* *104*, 163–175.
- 1094 Macdonald, R., Belkin, H., Fitton, J., Rogers, N., Nejbort, K., Tindle, A. & Marshall, A. (2008).
1095 The Roles of Fractional Crystallisation, Magma Mixing, Crystal Mush Remobilization and
1096 Volatile-Melt Interactions in the Genesis of a Young Basalt-Peralkaline Rhyolite Suite, the
1097 Greater Olkaria Volcanic Complex, Kenya Rift Valley. *Journal of Petrology* *49*(8), 1515-1547.
- 1098 Macdonald, R., Navarro, J., Upton, B. & Davies, G. (1994). Strong Compositional Zonation in
1099 Peralkaline Magma: Menengai, Kenya Rift Valley. *Journal of Volcanology and Geothermal*
1100 *Research* *60*, 301–325.
- 1101 Mahatsente, R., Jentzsch, G. & Jahr, T. (1999). Crustal structure of the Main Ethiopian Rift from
1102 gravity data: 3-dimensional modeling. *Tectonophysics* *313*, 363–382.
- 1103 Mahood, G., & Hildreth, W. (1986). Geology of the Peralkaline Volcano at Pantelleria, Strait of
1104 Sicily. *Bulliten of Volcanology* *48*(2-3), 143–172.
- 1105 Mahood, G. & Stimac, J. (1990). Trace-Element Partitioning in Pantellerites and Trachytes.
1106 *Geochemica et Cosmochimica Acta* *54*, 2257–2276.
- 1107 Manzella, A., Volpi, G., Zaja, A. & Meju, M. (2004). Combined TEM-MT Investigation of
1108 Shallow-Depth Resistivity Structure of Mt Somma-Vesuvius. *Journal of Volcanology and*
1109 *Geothermal Research* *131*(1), 19–32.
- 1110 Marshall, A., Macdonald, R., Rogers, N., Fitton, J., Tindle, A., Nejbort, K. & Hinton, R. (2009).
1111 Fractionation of Peralkaline Silicic Magmas: The Greater Olkaria Volcanic Complex, Kenya Rift
1112 Valley. *Journal of Petrology* *50*(2), 323–359.
- 1113 Mattia, M., Bonaccorso, A. & Guglielmino, F. (2007). Ground deformations in the Island of
1114 Pantelleria (Italy): Insights into the dynamic of the current intereruptive period. *Journal of*
1115 *Geophysical Research* *112*, B1406.
- 1116 Mazzarini, F., Corti, G., Manettie, P. & Innocenti, F. (2004). Strain Rate and Bimodal Volcanism
1117 in the Continental Rift: Debre Zeyt Volcanic Field, Northern MER, Ethiopia. *Journal of African*
1118 *Earth Sciences* *39*, 415–420.
- 1119 McKenzie, D. (1984). The Generation and Compaction of Partially Molten Rock. *Journal of*
1120 *Petrology* *25*, 713–765.
- 1121 Miller, D. & Smith, R. (1999). P and S Velocity Structure of the Yellowstone Volcanic Field
1122 from Local Earthquake and Controlled-Source Tomography. *Journal of Geophysical Research*
1123 *104*(B7) 15105–15121.
- 1124 Mohr, P. (1983). Perspectives on the Ethiopian Volcanic Province. *Bulliten of Volcanology*
1125 *46*(1), 23–43.

- 1126 Mushkin, M., Stein, M., Halicz, L. & Navon, O. (2002). The Daly Gap: Low-Pressure
1127 Fractionation and Heat-Loss From Cooling Magma Chamber. *Geochemica et Cosmochimica*
1128 *Acta* 66(15A), A539.
- 1129 Neave, D., Fabbro, G., Herd, R., Petrone, C. & Edmonds, M. (2012). Melting, Differentiation
1130 and Degassing at the Pantelleria Volcano, Italy. *Journal of Petrology* 53(3), 637–663.
- 1131 Neave, D. & Putirka, K. (2017). A New Clinopyroxene-Liquid Barometer, and Implications for
1132 Magma Storage Pressures Under Icelandic Rift Zones. *American Mineralogist* 102(4), 777–794.
- 1133 Nicholls, J. & Carmichael, J. (1969). Peralkaline Acid Liquids: A Petrological Study.
1134 *Contributions to Mineralogy and Petrology* 20, 268–294.
- 1135 Pagli, C., Wright, T.J., Ebinger, C.J., Yun, S.H., Cann, J.R., Barnie, T.L. & Ayele, A. (2012).
1136 Shallow axial magma chamber at the slow-spreading Erta Ale Ridge. *Nature Geoscience* 5(4),
1137 284–288.
- 1138 Peccerillo, A., Barberio, M., Yirgu, G., Ayalew, D., Barbieri, M. & Wu, T. (2003). Relationships
1139 between Mafic and Peralkaline Silicic Magmatism in Continental Rift Settings: A Petrological,
1140 Geochemical and Isotopic Study of the Gedemsa Volcano, Central Ethiopian Rift. *Journal of*
1141 *Petrology* 44(11), 2003–2032.
- 1142 Peccerillo, A., Mandefro, B., Solomon, G., Hambisa, G., Bedru, H. & Tesfaye, S. (1998). The
1143 Precambrian Rocks from Southern Ethiopia: Petrology, Geochemistry and Their Interaction with
1144 the Recent Volcanism from the Ethiopian Rift Valley. *Neues Jahrbuch Für Mineralogie-*
1145 *Abhandlungen*, 237–262.
- 1146 Pous, J., Queralt, P., Ledo, J. & Roca, E. (1999). A High Electrical Con-
1147 ductive Zone at Lower Crustal Depth beneath the Betic Chain (Spain). *Earth and Planetary Science Letters* 167, 35–45.
- 1148 Putirka, K. (2008). Thermometers and Barometers for Volcanic Systems. In K. D. Putirka & F. J.
1149 Tepley (Eds), *Minerals, Inclusions and Volcanic Processes*. *Mineralogical Society of America*
1150 *and Geochemical Society, Reviews in Mineralogy and Geochemistry* (Vol 69, pp. 61–120).
- 1151 Rabinowicz, M., Genthon, P., Ceuleneer, G. & Hillairret, M. (2001). Compaction in a Mantle
1152 Mush with High Melt Concentrations and the Generation of Magma Chambers. *Earth and*
1153 *Planetary Science Letters* 188, 313–328.
- 1154 Rampey, M., Oppenheimer, C., Pyle, D. & Yirgu, G. (2010). Caldera-Forming Eruptions of the
1155 Quaternary Kone Volcanic Complex, Ethiopia. *Journal of African Earth Sciences* 58, 51–66.
- 1156 Rampey, M., Oppenheimer, C., Pyle, D. & Yirgu, G. (2014). Physical Volcanology of the
1157 Gubisa Formation, Kone Volcanic Complex, Ethiopia. *Journal of African Earth Sciences* 96,
1158 212–219.
- 1159 Ronga, F., Lustrino, M., Marzoli, A. & Melluso, L. (2010). Petrogenesis of a Basalt-Comendite-
1160 Pantellerite Rock Suite: The Boseti Volcanic Complex (Main Ethiopian Rift). *Mineralogy and*
1161 *Petrology* 98, 227–243.
- 1162 Rooney, T., Bastow, I. & Keir, D. (2011). Insights into Extensional Processes during Magma
1163 Assisted Rifting: Evidence from Aligned Scoria Cones. *Journal of Volcanology and Geothermal*
1164 *Research* 201(1-4), 83-96.

- 1165 Rooney, T., Furman, T., Bastow, I.D., Ayalew, D. & Yirgu, G. (2007). Lithospheric modification
1166 during crustal extension in the Main Ethiopian Rift. *Journal of Geophysical Research* 112.
- 1167 Rooney, T., Hart, W., Hall, C., Ayalew, D., Ghiorso, M., Hidalgo, P. & Yirgu, G. (2012).
1168 Peralkaline Magma Evolution and the Tephra Record in the Ethiopian Rift. *Contributions to*
1169 *Mineralogy and Petrology* 164, 407–426.
- 1170 Ruprecht, P. & Bachmann, O. (2010). Pre-Eruptive Reheating during Magma Mixing at Quizapu
1171 Volcano and the Implications for the Explosiveness of Silicic Arc Volcanoes. *Geology* 38(10),
1172 919–922.
- 1173 Samrock, F., Kushinov, A., Bakker, J., Jackson, A. & Fisseha, S. (2015). 3-D Analysis and
1174 Interpretation of Magnetotelluric Data from the Aluto-Langano Geothermal Field, Ethiopia.
1175 *Geophysical Journal International* 202(3), 1923–1948.
- 1176 Saria, E., Calais, E., Stamps, D., Delvaux, D. & Hartnady, C. (2014). Present-Day Kinematics of
1177 the East African Rift. *Journal of Geophysical Research: Solid Earth* 119(4), 3584–3600.
- 1178 Scaillet, B., Holtz, F. & Pichavant, M. (1998). Phase Equilibrium Constraints on the Viscosity of
1179 Silicic Magmas 1. Volcanic–plutonic Comparison. *Journal of Geophysical Research* 103,
1180 27257–27266.
- 1181 Schilling, F. & Partzsch, G. (2001). Quantifying Partial Melt Portion in the Crust beneath the
1182 Central Andes and the Tibetan Plateau. *Physics and Chemistry of the Earth, Part A* 26, 239–246.
- 1183 Schindelin, J., Arganda-Carreras, I., Frise, E., Kaynig, V., Longair, M., Pietzsch, T., Preibisch,
1184 S., et al. (2012). Fiji: an open-source platform for biological-image analysis, *Nature*
1185 *methods* 9(7), 676–682
- 1186 Shand, S. (1998). On the relations between silica, alumina, and the bases in eruptive rocks,
1187 considered as a means of classification. *Geological Magazine* 64(10), 446–449.
- 1188 Shirley, D. (1986). Compaction in Igneous Cumulates. *Journal of Geology* 94,795–809.
- 1189 Steck, L., Thurber, C., Fehler, M., Lutter, W., Roberts, P., Baldrige, W., Stafford, D., et al.
1190 (1998). Crust and Upper Mantle P Wave Velocity Structure beneath Valles Caldera, New
1191 Mexico: Results from the Jemez Teleseismic Tomography Experiment. *Journal of Geophysical*
1192 *Research* 103(B10), 24301–24320.
- 1193 Stevenson, R. & Wilson, L. (1997). Physical Volcanology and Eruption Dynamics of Peralkaline
1194 Agglutinates from Pantelleria. *Journal of Volcanology and Geothermal Research* 79(1-2), 97–
1195 122.
- 1196 Thompson, R. & MacKenzie, W. (1990). Feldspar-Liquid Equilibria in Peralkaline Acid Liquids:
1197 An Experimental Study. *American Journal of Science* 265, 714–734.
- 1198 Thy, P., Beard, J. & Lofgren, G. (1990). Experimental Constraints on the Origin of Icelandic
1199 Rhyolites. *Journal of Geology* 98, 417–421.
- 1200 Trua, T., Deniel, C. & Mazzuoli, R. (1999). Crustal Control in the Genesis of Plio-Quaternary
1201 Bimodal Magmatism of the Main Ethiopian Rift (MER): Geochemical and Isotopic (Sr, Nd, Pb)
1202 Evidence. *Chemical Geology* 155, 201–231.

- 1203 Tyburezy, J. & Waff, H. (1985). High Pressure Electrical Conductivity in Naturally Occurring
1204 Silicate Liquids. In R. N. Shock (Ed.), *Point Defects in Minerals, Geophysical Monograph*
1205 *Series* (Vol. 1, pp. 78–87). Washington, D. C.: American Geophysical Union.
- 1206 Vigneresse, J., Barbey, P. & Cuney, M. (1996). Rheological Transitions During Partial Melting
1207 and Crystallisation with Application to Felsic Magma Segregation and Transfer. *Journal of*
1208 *Petrology* 37(6), 1579–1600.
- 1209 Waff, H. & Weill, D. (1975). Electrical Conductivity of Magmatic Liquids: Effects of
1210 Temperature, Oxygen Fugacity and Composition. *Earth and Planetary Science Letters* 28, 254–
1211 260.
- 1212 Wark, D., Hildreth, W., Spear, F., Cherniak, D. & Watson, E. (2007). Pre-Eruption Recharge of
1213 the Bishop Magma System. *Geology* 35(3), 235–238.
- 1214 Webster, J., Taylor, R. & Bean, C. (1993). Pre-Eruptive Melt Composition and Constraints on
1215 Degassing of a Water-Rich Pantellerite Magma, Fantale Volcano, Ethiopia. *Contributions to*
1216 *Mineralogy and Petrology* 114, 53–62.
- 1217 Whaler, K. & Hautot, S. (2006). The Electrical Resistivity Structure of the Crust beneath the
1218 Northern Main Ethiopian Rift. *Geological Society, London, Special Publications* 259, 293–305.
- 1219 White, J.C., Holt, G.S., Parker, D.F. & Ren, M. (2003). Trace-element partitioning between
1220 alkali feldspar and peralkalic quartz trachyte to rhyolite magma. Part I: Systematics of trace-
1221 element partitioning. *American Mineralogist* 88, 316–329.
- 1222 White, J.C., Parker, D.F. & Minghua, R. (2009). The origin of trachyte and pantellerite from
1223 Pantelleria, Italy: Insights from major element, trace element, and thermodynamic modelling.
1224 *Journal of Volcanology and Geothermal Research* 179, 33–55.
- 1225 Wilks, M., Kendall, J., Nowacki, A., Biggs, J., Wookey, J., Birhanu, Y., Atalay, A., et al. (2017).
1226 Seismicity Associated with Magmatism, Faulting and Hydrothermal Circulation at Aluto
1227 Volcano, Main Ethiopian Rift. *Journal of Volcanology and Geothermal Research* 340, 52–67.
- 1228 Williams, F.M., Williams, M.A.J. & Aumento, F. (2004). Tensional fissures and crustal
1229 extension rates in the northern part of the Main Ethiopian Rift. *Journal of African Earth Sciences*
1230 38, 183–197.
- 1231 WoldeGabriel, G., Aronson, J. & Walter, R. (1990). Geology, Geochronology, and Rift Basin
1232 Development in the Central Sector of the Main Ethiopia Rift. *Geological Society of America*
1233 *Bulletin* 102, 439–458.
- 1234 Wotzlaw, J., Bindeman, I., Watts, K., Schmitt, A., Caricchi, L. & Schaltegger, U. (2014).
1235 Linking Rapid Magma Reservoir Assembly and Eruption Trigger Mechanisms at Evolved
1236 Yellowstone-Type Supervolcanoes. *Geology* 42(9), 807–810.
- 1237 Xu, W., Rivalta, E. & Ling, X. (2017). Magmatic architecture within a rift segment: Articulate
1238 axial magma storage at Erta Ale volcano, Ethiopia. *Earth and Planetary Science Letters* 476, 79–
1239 86.
- 1240 Zandt, G., Leidig, M., Chmielowski, J., Baumont, D. & Yuan, X. (2003). Seismic Detection and
1241 Characterization of the Altiplano-Puna Magma Body, Central Andes. *Pure and Applied*
1242 *Geophysics* 160(3-4), 789–807.

1243 **Table 1:** Selected whole-rock data for Kone and Fentale volcanoes acquired via XRF analysis at the Department of Geology at the University of Leicester. LOI=
1244 loss on ignition; bdl = below detection limit; A.I. = agpaite index (molar (Na₂O+K₂O)/Al₂O₃).

1245

Sample	Kone3.9	Kone3.18	Kone3.30	Kone3.41	Kone4.10	K04	K05	K06	K07	KoneBG25	KoneBN29	MER128A	MER130A	MER133A	
Rock Type	Pumice airfall	Pumice airfall	Porphyritic obsidian	Pumice airfall	Porphyritic obsidian	Porphyritic obsidian	Ignimbrite	Pumice lapilli	Porphyritic obsidian	Porphyritic obsidian	Welded ignimbrite	Pumice lapilli breccia	Pumice lapilli breccia	Basalt scoria	
Relative Age	Kone caldera	Kone caldera	Post-Kone caldera	Kone caldera	Pre-Kone caldera	Pre-Birenti caldera	Birenti caldera	Post-Kone caldera	Post-Kone caldera	Pre-Kone caldera	Kone caldera	Kone caldera	Kone caldera	Post-Kone caldera	
Location	Lat. (N)	8.8178	8.8280	8.8691	8.8244	8.8628	8.7875	8.7875	8.8156	8.8158	Northwest rim of Kone caldera	South wall Kone caldera	8.7877	8.8091	8.8544
	Long. (E)	39.6769	39.6538	39.7250	39.6591	39.6640	39.7383	39.7383	39.6995	39.7008			39.6589	39.6873	39.7469
SiO₂	wt%	66.20	66.73	70.01	72.01	70.15	70.14	70.28	72.69	71.64	70.73	66.71	65.24	69.36	46.40
TiO₂	wt%	0.40	0.29	0.46	0.23	0.39	0.46	0.48	0.21	0.23	0.39	0.47	0.51	0.23	1.99
Al₂O₃	wt%	10.90	7.45	9.30	10.27	7.93	9.32	10.18	8.11	8.42	7.89	11.39	8.95	8.40	15.14
FeO_T	wt%	6.56	8.52	8.34	4.54	9.16	7.92	8.27	8.57	7.97	8.98	7.00	7.67	6.28	12.04
MnO	wt%	0.24	0.29	0.28	0.14	0.30	0.30	0.30	0.31	0.29	0.33	0.30	0.30	0.23	0.18
MgO	wt%	0.06	0.08	0.03	0.08	0.04	0.02	0.11	0.07	0.07	0.04	0.09	0.28	0.16	8.42
CaO	wt%	0.45	0.38	0.38	0.28	0.38	0.41	0.88	0.60	0.34	0.36	0.59	1.80	0.62	10.15
Na₂O	wt%	4.57	6.43	6.39	4.63	6.67	6.49	5.64	3.12	6.76	6.68	6.05	3.63	3.90	2.84
K₂O	wt%	4.95	4.69	4.40	4.94	4.32	4.37	4.08	5.65	4.16	4.29	4.64	5.09	5.52	0.85
P₂O₅	wt%	0.03	0.03	0.03	0.02	0.03	0.02	0.03	0.02	0.02	0.02	0.04	0.03	0.02	0.51
LOI	wt%	3.44	3.48	-0.27	2.26	-0.36	-0.01	0.06	0.24	-0.01	-0.34	2.18	5.44	4.28	0.25
Total	wt%	99.17	98.38	98.85	99.40	99.03	99.45	100.29	99.59	99.90	99.39	99.48	98.98	99.02	98.77
A.I.		1.18	2.10	1.64	1.26	1.97	1.65	1.35	1.39	1.86	1.98	1.32	1.28	1.47	0.37

Ba	ppm	176.7	95.6	53.1	39.2	79.0	64.6	146.7	248.8	220.6	83.6	591.6	65.5	30.4	395.5
Ce	ppm	214.3	275.7	206.8	203.4	295.7	220.9	246.0	334.7	274.6	329.0	192.1	208.0	471.1	52.0
Co	ppm	2.4	3.7	5.2	1.5	4.3	3.6	1.5	3.4	2.6	4.7	5.0	4.8	5.0	51.7
Cr	ppm	bdl	bdl	bdl	bdl	bdl	bdl	bdl	bdl	bdl	bdl	bdl	bdl	bdl	326.1
La	ppm	102.2	120.9	100.9	97.1	139.7	110.5	125.2	166.5	135.4	153.8	92.9	99.0	227.6	22.6
Nb	ppm	156.0	209.7	143.0	132.6	223.6	145.1	158.2	215.0	179.3	228.5	125.7	127.6	325.8	29.6
Ni	ppm	bdl	bdl	bdl	bdl	bdl	bdl	bdl	bdl	bdl	bdl	bdl	2.1	5.6	121.1
Rb	ppm	124.6	162.2	142.7	178.6	168.5	145.4	132.9	220.1	161.2	173.6	102.7	131.1	332.2	14.7
Sr	ppm	5.3	11.5	3.8	10.0	6.4	0.60	23.8	37.9	6.1	6.0	10.8	81.0	27.4	427.1
Th	ppm	16.9	21.1	18.2	20.2	23.5	18.0	18.3	25.7	20.7	23.6	13.6	14.8	45.3	1.9
Y	ppm	118.9	170.1	117.5	99.1	175.4	120.1	84.4	188.1	152.5	179.6	100.9	110.5	243.3	30.4
Zr	ppm	1029.7	1324.6	947.0	882.1	1411.6	1006.2	1077.4	1486.2	1215.9	1447.9	832.9	836.8	2141.9	152.0

Sample	MER136A	MER137A	MER138A	MER140Bb	F01	F03	F12	F16	F27	F41	F44	F48	F49	
Rock Type	Basalt scoria	Basalt scoria	Basalt scoria	Welded ignimbrite	Porphyritic obsidian	Pumice lapilli	Basaltic scoria	Porphyritic obsidian	Porphyritic obsidian	Pumice lapilli	Welded ignimbrite	Welded ignimbrite	Basalt scoria	
Relative Age	Post-Kone caldera	Post-Kone caldera	Post-Kone caldera	Kone caldera	Pre-caldera	Pre-caldera	Post-caldera	Post-caldera	Pre-caldera	Post-caldera	Caldera	Caldera	Post-caldera	
Location	Lat. (N)	8.8239	8.8292	8.8418	8.8434	8.9978	8.9978	8.9381	8.9584	8.9776	8.9578	8.9577	8.9279	8.9525
	Long. (E)	39.7047	39.7096	39.7139	39.7332	39.8709	39.8709	39.8927	39.9271	39.8733	39.8992	39.8986	39.8432	39.7550
SiO₂	wt%	46.48	46.32	46.25	72.07	69.56	70.11	46.94	71.65	69.63	71.76	69.24	69.98	46.45
TiO₂	wt%	2.23	2.17	2.29	0.37	0.52	0.50	3.92	0.38	0.48	0.35	0.51	0.42	2.44
Al₂O₃	wt%	14.65	14.54	14.71	10.09	9.59	9.32	13.62	9.41	8.23	8.99	9.83	9.15	15.58
FeO_T	wt%	12.60	12.54	12.60	6.34	8.42	8.36	15.51	7.40	9.40	7.45	8.65	8.47	13.03
MnO	wt%	0.19	0.19	0.19	0.22	0.36	0.33	0.28	0.28	0.40	0.28	0.33	0.33	0.18
MgO	wt%	8.81	9.23	8.58	0.10	0.02	0.07	4.78	0.20	0.05	0.06	0.18	0.11	8.26
CaO	wt%	10.55	10.51	10.68	0.37	0.47	0.86	9.04	0.81	0.41	0.41	0.72	0.54	10.44
Na₂O	wt%	3.10	2.93	3.09	5.49	6.82	5.44	3.96	6.29	6.83	5.83	6.50	6.40	2.95
K₂O	wt%	0.97	0.92	0.99	4.43	4.13	4.54	0.89	3.80	4.19	4.21	3.99	4.26	0.73
P₂O₅	wt%	0.52	0.48	0.55	0.03	0.03	0.03	1.18	0.07	0.03	0.02	0.05	0.03	0.45
LOI	wt%	-0.55	-0.36	-0.32	0.18	-0.02	0.18	-0.03	-0.01	-0.02	0.13	0.07	0.13	0.50
Total	wt%	99.58	99.50	99.61	99.67	99.91	99.75	100.20	100.28	99.69	99.55	100.07	99.86	101.01
A.I.		0.42	0.40	0.42	1.37	1.64	1.49	0.55	1.54	1.92	1.57	1.53	1.65	0.36

Ba	ppm	391.3	364.6	425.7	208.6	637.2	702.0	474.2	269.2	769.9	422.5	614.0	530.2	274.6
Ce	ppm	62.8	59.0	63.4	275.9	240.6	259.7	68.2	319.5	266.1	320.8	239.7	255.7	46.3
Co	ppm	51.5	52.9	48.9	4.2	3.8	2.0	27.2	3.3	3.0	4.2	2.1	2.9	48.1
Cr	ppm	386.1	435.7	351.5	bdl	bdl	bdl	6.7	bdl	bdl	bdl	bdl	bdl	219.5
La	ppm	32.1	24.7	31.0	127.5	119.3	130.2	30.1	160.4	132.2	158.1	116.3	127.8	20.6
Nb	ppm	39.4	36.5	41.6	192.1	159.6	164.9	36.5	226.6	174.8	208.2	156.2	166.6	26.6
Ni	ppm	137.4	157.4	123.3	bdl	bdl	bdl	bdl	bdl	bdl	bdl	bdl	bdl	56.2
Rb	ppm	25.1	22.8	25.6	167.4	119.5	128.1	18.7	162.0	123.1	153.1	117.5	128.3	13.9
Sr	ppm	577.2	551.8	596.7	15.5	7.3	37.6	502.1	43.7	12.8	12.1	27.5	18.9	507.0
Th	ppm	2.8	2.9	3.4	23.7	15.4	15.8	23.0	23.0	15.2	20.6	15.3	16.3	1.5
Y	ppm	27.5	26.6	28.6	125.5	133.4	143.6	44.3	169.3	153.2	175.1	128.2	140.9	25.2
Zr	ppm	161.8	151.6	167.0	1240.3	1020.1	1057.3	168.3	1431.9	1092.9	1391.0	1023.6	1100.5	142.9

1246 **Table 2:** Selected glass data for Aluto, Kone, and Fentale volcanoes. Major elements were acquired via EPMA at the Department of Earth Sciences at the
 1247 University of Cambridge, trace elements were acquired via SIMS at the School of Geosciences at the University of Edinburgh. bdl = below detection limit; A.I. =
 1248 agpaite index (molar (Na₂O+K₂O)/Al₂O₃).

Sample	01-02-24	13-05-04	26-01-SMP	31-01-LE	F01	F11	F16	F17	F27	F42	F44	F48	K3.9	K3.18	
Rock type	Porphyritic obsidian	Welded ignimbrite	Porphyritic obsidian	Porphyritic obsidian	Porphyritic obsidian	Welded ignimbrite	Porphyritic obsidian	Pumice lapilli	Porphyritic obsidian	Pumice lapilli	Welded ignimbrite	Welded ignimbrite	Pumice lapilli	Pumice lapilli	
Relative age	Post-caldera	Caldera	Post-caldera	Post-caldera	Pre-caldera	Caldera	Post-caldera	Post-caldera	Pre-caldera	Post-caldera	Caldera	Caldera	Kone caldera	Kone caldera	
Location	Lat. (N)	7.7698	7.8407	7.8161	7.7832	8.9978	8.9378	8.9584	8.9535	8.9776	8.9578	8.9577	8.9279	8.8178	8.8280
	Long. (E)	38.7471	38.7303	38.7773	38.8268	39.8709	39.8934	39.9271	39.9295	39.8733	39.8992	39.8986	39.8432	39.6769	39.6538
SiO ₂	wt%	74.16	73.02	73.36	74.02	70.67	69.78	70.37	72.65	70.54	73.12	71.42	70.34	74.97	75.15
TiO ₂	wt%	0.28	0.31	0.16	0.26	0.55	0.49	0.20	0.51	0.54	0.53	0.42	0.31	0.14	0.15
Al ₂ O ₃	wt%	10.16	9.20	8.95	9.09	9.58	9.48	11.98	8.87	9.48	9.11	8.76	11.20	8.68	8.79
FeO	wt%	5.33	6.49	6.86	6.27	8.03	8.69	5.31	7.60	8.09	7.54	8.22	6.23	6.12	6.19
MnO	wt%	0.27	0.26	0.38	0.33	0.43	0.39	0.23	0.36	0.41	0.35	0.39	0.29	0.32	0.32
MgO	wt%	bdl	0.02	bdl	bdl	0.02	0.01	0.03	0.01	0.01	bdl	0.02	0.02	0.02	bdl
CaO	wt%	0.20	0.19	0.20	0.23	0.28	0.52	0.15	0.41	0.33	0.37	0.35	0.21	0.19	0.20
Na ₂ O	wt%	5.11	4.87	5.66	5.22	5.71	6.10	6.35	5.24	5.88	4.67	5.89	6.20	5.20	4.79
K ₂ O	wt%	4.50	5.65	4.42	4.53	4.60	4.39	5.33	4.32	4.63	4.31	4.48	5.11	4.36	4.39
P ₂ O ₅	wt%	bdl	bdl	0.02	0.05	0.13	0.16	0.04	0.02	0.10	bdl	0.07	0.06	bdl	0.03
A.I.		1.31	1.54	1.57	1.49	1.50	1.56	1.35	1.50	1.55	1.36	1.66	1.40	1.10	1.05
Ba	ppm	367.2	107.9	393.4	370.5	694.2	679.5	292.3	853.3	856.9	482.1	652.6	525.7	247.3	246.0
Ce	ppm	198.9	290.7	324.8	267.1	210.2	190.4	323.8	270.0	236.3	299.5	200.5	239.0	357.3	347.8
La	ppm	98.5	149.4	162.1	134.1	104.9	91.6	166.5	136.8	117.9	151.3	99.2	122.7	177.6	172.4
Nb	ppm	132.9	240.5	212.8	177.8	152.5	124.6	258.5	179.2	163.1	212.8	137.3	165.3	230.1	230.3
Rb	ppm	101.1	117.7	147.9	126.6	118.9	17.1	198.7	141.2	126.5	168.8	114.3	128.6	147.3	146.2
Sr	ppm	4.7	4.3	6.8	5.8	8.3	9.5	14.6	10.9	13.2	12.5	10.0	9.7	4.5	4.3
Y	ppm	97.8	120.0	158.8	130.3	121.9	102.4	186.0	147.1	140.1	169.6	115.4	140.3	157.0	154.0
Zr	ppm	814.2	1387.5	1319.4	1085.7	890.0	780.1	1495.6	1019.4	952.6	1304.9	816.8	1007.1	1362.1	1371.0

1249

Sample	K3.30	K3.41	K4.10	K06	KBG25	KBN29	M057A	MER128A	M130A	MER133A	MER136A	MER137A	MER138A	MER140Bb	
Rock type	Porphyritic obsidian	Pumice airfall	Porphyritic obsidian	Pumice lapilli	Porphyritic obsidian	Welded ignimbrite	Pumice lapilli	Pumice lapilli breccia	Pumice lapilli breccia	Basalt scoria	Basalt scoria	Basalt scoria	Basalt scoria	Welded ignimbrite	
Relative age	Post-Kone caldera	Kone caldera	Pre-Kone caldera	Post-Kone caldera	Pre-Kone caldera	Kone caldera	Post-caldera	Kone caldera	Kone caldera	Post-Kone caldera	Post-Kone caldera	Post-Kone caldera	Post-Kone caldera	Kone caldera	
Location	Lat. (N)	8.8691	8.8244	8.8628	8.8156	8.8000	8.8000	7.7865	8.7877	8.8091	8.8544	8.8239	8.8292	8.8418	8.8434
	Long. (E)	39.7250	39.6591	39.6640	39.6995	39.6920	39.6920	38.8098	39.6589	39.6873	39.7469	39.7047	39.7096	39.7139	39.7332
SiO₂	wt%	70.53	75.22	71.36	72.91	70.75	70.43	75.37	75.55	75.45	48.95	47.40	47.69	47.56	73.17
TiO₂	wt%	0.49	0.18	0.39	0.22	0.35	0.48	0.30	0.19	0.18	2.54	3.14	2.72	2.94	0.24
Al₂O₃	wt%	10.39	9.65	8.58	7.89	9.86	10.97	8.75	9.24	8.78	14.39	14.68	15.83	15.09	9.05
FeO	wt%	7.41	5.11	8.50	7.78	7.50	7.26	6.14	5.91	6.01	11.84	12.73	11.88	12.39	6.46
MnO	wt%	0.31	0.18	0.36	0.32	0.35	0.33	0.30	0.26	0.32	0.18	0.26	0.24	0.24	0.25
MgO	wt%	bdl	bdl	0.03	0.01	0.03	0.04	bdl	bdl	bdl	6.71	5.14	5.00	4.98	0.02
CaO	wt%	0.37	0.19	0.37	0.25	0.33	0.40	0.20	0.21	0.19	11.35	10.48	10.60	10.60	0.21
Na₂O	wt%	5.89	5.03	5.95	6.23	6.11	5.31	4.75	4.42	4.73	2.45	3.90	4.04	4.01	5.61
K₂O	wt%	4.55	4.44	4.42	4.39	4.66	4.65	4.20	4.23	4.32	0.99	1.51	1.39	1.44	4.91
P₂O₅	wt%	0.06	bdl	0.05	bdl	0.06	0.12	bdl	bdl	0.02	0.61	0.76	0.62	0.76	0.08
A.I.		1.01	0.98	1.21	1.35	1.09	0.91	1.41	0.94	1.03	0.24	0.37	0.34	0.36	1.16
Ba	ppm	72.5	24.8	96.8	298.9	95.7	455.7	245.2	153.1	215.1	447.2	513.8	467.1	513.7	59.9
Ce	ppm	181.7	255.9	268.8	316.2	268.5	203.5	298.6	318.7	196.1	64.5	91.6	79.1	86.4	290.7
La	ppm	91.4	131.8	136.3	159.4	134.4	102.7	147.2	160.5	97.2	29.1	44.3	40.3	43.1	149.0
Nb	ppm	130.3	202.7	209.1	216.6	207.5	148.7	200.3	229.3	130.8	32.6	53.0	43.9	49.8	225.3
Rb	ppm	156.5	261.9	192.3	214.3	194.8	152.1	151.4	240.0	89.0	22.8	38.7	32.2	36.4	245.1
Sr	ppm	2.2	5.1	4.7	8.5	4.7	4.9	4.5	4.2	3.3	580.4	590.0	625.6	624.8	2.7
Y	ppm	102.1	138.8	158.3	175.2	158.2	104.3	132.8	154.0	91.0	30.4	37.1	30.8	34.6	159.5
Zr	ppm	828.2	1202.1	1296.4	1353.9	1287.8	903.4	1131.9	1374.3	768.6	158.1	224.0	191.5	210.7	1395.3

1250

Sample	n	X _{An} , X _{Ab} , X _{Or}	Concentration (ppm)				Partition Coefficients	
			Ba mean	Ba min	Ba max	Ba σ	D _{Ba}	σ
Plagioclase								
13-05-04	1	An(37-42), Ab(60-56), Or(3-3)	2002	1691	2313	440	N/A	N/A
18-11-07	45	An(5-39), Ab(77-58), Or(3-24)	2875	920	4061	775	N/A	N/A
MER140Bb	3	An(11-20), Ab(73-72), Or(8-18)	3439	3114	3745	316	N/A	N/A
Alkali feldspar								
31-01-LE	6	An(0.1-0.4), Ab(65-58), Or(35-65)	1216	676	2443	496	3.56	1.52
26-01-SMP	10	An(0.1-0.3), Ab(60-50), Or(40-50)	800	489	2230	290	2.16	0.44
13-05-04	12	An(0.1-3), Ab(68-57), Or(32-43)	466	182	2350	421	6.37	5.12
F01	7	An(0.2-0.5), Ab(71-69), Or(28-31)	1535	1218	1987	267	2.35	0.33
F16	7	An(0.1-0.2), Ab(63-55), Or(37-45)	562	244	872	190	2.07	0.68
F27	15	An(0.1-0.5), Ab(71-66), Or(28-33)	1196	769	2681	303	1.39	0.35
F44	12	An(0.1-2), Ab(76-61), Or(24-39)	1467	405	4064	853	2.80	1.4
F48	6	An(0.1-1), Ab(73-63), Or(26-37)	1041	347	2061	653	2.83	1.2
K04	2	An(0.3-0.3), Ab(70-68), Or(30-32)	575	420	728	160	N/A	N/A
K05	3	An(0.1-0.3), Ab(68-66), Or(30-34)	443	309	778	155	N/A	N/A
KBN29	21	An(0.2-3), Ab(71-64), Or(29-35)	1477	835	2790	410	3.06	0.92
M057A	3	An(0.1-0.4), Ab(62-54), Or(38-46)	680	510	923	149	3.24	0.47
M140Bb	2	An(0.1-0.1), Ab(66-60), Or(34-40)	637	331	1044	340	9.35	5.41

1251 **Table 3:** Selected feldspar data for Aluto, Kone, and Fentale volcanoes acquired via EPMA at the Department of
 1252 Earth Sciences at the University of Cambridge. Partition coefficients given are the average ‘apparent’ partition
 1253 coefficients calculated from feldspar rim and corresponding glass compositions. n = number of crystals analysed
 1254 (typically one analysis of plagioclase crystals, two analyses representing core and rim sections of the crystal for
 1255 alkali feldspars); X_{An} = anorthoclase content; X_{Ab} = albite content; X_{Or} = orthoclase content; N/A = partition
 1256 coefficients not calculated (due to lack of glass and/or feldspar rim compositions).

1257 **Figure 1: a)** Map locating the Main Ethiopian Rift **(b)** within the larger eastern branch of the East African Rift
 1258 system. Peralkaline calderas are outlined in dark blue, with Quaternary eruption deposits highlighted in white (Corti,
 1259 2008). The red lines represent the Wonji Fault Belt, where the majority of extensional stress is accommodated; the
 1260 black lines represent the older, less active border faults (Corti, 2008). Aluto volcano is located at the southern end of
 1261 the central Main Ethiopian Rift, Kone and Fentale are located at the northern end; simplified geological maps
 1262 (adapted from Hutchison et al., 2016c; Rampey et al., 2010; Gibson, 1974) are shown for both **(c, d and e,**
 1263 **respectively).**

1264

1265 **Figure 2:** QEMSCAN phase assemblage maps showing key petrological textures. The QEMSCAN software creates
 1266 phase assemblage maps from data acquired from a combination of low-count energy-dispersive X-ray spectra
 1267 (EDX) and BSE brightness and X-ray count information. From top left to bottom right- a) Fe chemical map
 1268 displaying the phase assemblage and petrological textures of a post-caldera basaltic scoria from Kone. Note the
 1269 glomerocrystic clotting of phenocrysts, and zoned olivines (red) and clinopyroxene (green); b) Crystal-rich trachytic
 1270 ignimbrite from Aluto, dominated by anorthoclase. Some crystals are normally zoned with plagioclase cores.
 1271 Fayalite, aegirine augite, and microphenocrysts of Fe-Ti oxides form glomerocrystic clots with the feldspar. Quartz
 1272 completes the assemblage; all is set in a devitrified groundmass; c) Crystal-rich rhyolitic ignimbrite from Kone,

1273 showing a large fiamme on the right. Dominated by anorthoclase, quartz, aegirine-augite and aenigmatite complete
 1274 the phase assemblage, all set in a devitrified groundmass; d) Pumice lapillus from a fall deposit from Kone
 1275 associated with the caldera formation. The phase assemblage present is similar to related ignimbrites, dominated by
 1276 anorthoclase. Aegirine augite and microphenocrysts of Fe-Ti oxides form glomerocrystic clots to give a similar
 1277 texture; e) Trachytic pre-caldera lava from Kone, dominated by anorthoclase. Aegirine augite and Fe-Ti oxides are
 1278 also present, forming glomerocrystic clots with the feldspar crystals. The fine-medium groundmass is dominated by
 1279 quartz, alkali feldspar and aegirine augite; f) A comparatively more crystal-poor rhyolitic lava from Aluto. The
 1280 phase assemblage is dominated by anorthoclase, aenigmatite and aegirine augite. Complex granophyric intergrowths
 1281 of alkali feldspar and quartz are common.

1282

1283 **Figure 3:** Whole-rock analyses of Kone and Fentale samples. Dashed fields show Aluto data coverage (Hutchison et
 1284 al., 2016c), glass analyses for the three volcanoes are shown by unfilled symbols- **a)** Total alkalis versus silica
 1285 (TAS) diagram. The dashed line shows the alkaline-sub-alkaline divide of Irvine and Baragar (1971); **b)**
 1286 Classification diagram of peralkaline rhyolites and trachytes (Macdonald, 1974). Colours are used to denote the
 1287 three different volcanoes throughout the paper, shapes the relative age of deposits. Errors are smaller than symbols
 1288 shown.

1289

1290 **Figure 4:** Harker variation diagrams of whole-rock and glass major element compositions. Dashed fields show
 1291 Aluto whole-rock data coverage (Hutchison et al., 2016c), solid lines show melt composition predicted by the best-
 1292 fit RhyoliteMELTS models (Gleeson et al., 2017; Gualda et al., 2012). Errors are smaller than symbols shown.

1293

1294 **Figure 5:** Whole-rock and glass trace element compositions plotted against Zr concentration due to its
 1295 incompatibility **(a)**. Dashed fields show Aluto whole-rock data coverage (Hutchison et al., 2016c), shaded field
 1296 shows Precambrian crustal rock geochemistry (Peccerillo et al., 1998), which likely represent a component of the
 1297 basement rocks. Key as in **figure 3**. Errors are smaller than symbols shown.

1298

1299 **Figure 6:** Feldspar classification ternary diagram, solid lines show feldspar compositions predicted by the best-fit
 1300 RhyoliteMELTS models (Gleeson et al., 2017; Gualda et al., 2012).

1301

1302 **Figure 7:** Feldspar trace element compositions are highly variable, to investigate the presence/absence of zoning
 1303 plot a) shows Ba and Or concentration in the core of the alkali feldspar normalised by the concentration of Ba and Or
 1304 in the rim, whilst b) shows selected Ba profiles across a number of crystals from Kone, Fentale and Aluto. Key as in
 1305 **figure 6**.

1306

1307 **Figure 8:** Melt SiO₂ predicted by best-fit RhyoliteMELTS models (Gualda et al., 2012) for Kone and Fentale
 1308 volcanoes against **(a)** the predicted melt temperature, **(b)** the predicted liquid fraction (F), and **(c)** the relative rates
 1309 of differentiation (change in silica content with respect to time), estimated from RhyoliteMELTS output at wall rock
 1310 temperatures of 500 °C (solid lines) and 700 °C (dashed lines).

1311

1312 **Figure 9:** Plot showing observed feldspar Ba contents against observed glass Ba contents. Partition coefficients
 1313 calculated based on the experimental work of Henderson and Pirozynski (2012) have been used to predict glass Ba
 1314 concentrations based on feldspar rim compositions (solid lines). Dashed lines show where adjusted values of NKA
 1315 have been used in the calculation due to probable Na₂O loss. Melt Ba contents based on the observed partition
 1316 coefficients of Mahood and Stimac (1990) are also indicated by the thick solid lines. Errors in feldspar Ba content
 1317 are displayed by horizontal lines, errors in glass Ba content were smaller than the symbols shown.

1318

1319 **Figure 10:** Plots showing (a) feldspar and (b) glass Ba concentrations against glass SiO₂. ‘Apparent’ feldspar-melt
1320 Ba partition coefficients are shown against glass SiO₂ (c) and NKA (d). Solid lines depict the result of models based
1321 on the liquid line of descent from best-fit RhyoliteMELTS models (Gleeson et al., 2017; Gualda et al., 2012) in
1322 tandem with a parameterisation of the feldspar-melt partition coefficient based on peralkalinity and temperature
1323 (after Henderson & Pirozynski, 2012). Thick black lines (c and d) represent the minimum and maximum observed
1324 partition coefficients presented by Mahood and Stimac (1990). Experimental data from Henderson and Pirozynski
1325 (2012) is also plotted, along with observed values from Mahood and Stimac (1990).

1326

1327 **Figure 11:** Schematic showing the hypothesised structure of peralkaline magma reservoirs beneath MER
1328 volcanoes. Peralkaline magmas are fed by a mafic melts that undergo protracted fractional crystallisation. The
1329 shallow reservoir is dominated by a feldspar-rich mush, built up by crystal-melt segregation, aided by the low-
1330 viscosity of peralkaline melts. Feldspar crystallisation steadily strips the residual melts of compatible trace elements,
1331 such as Ba, leading to a compositional stratification of the mush pile. During explosive caldera-forming eruptions
1332 crystals are scavenged from deep in this mush pile, leading to the incorporation of feldspar crystals that are too Ba-
1333 enriched to be in equilibrium with their carrier melts. Post-caldera eruptions primarily tap residual melt lenses and
1334 do not appear to incorporate significant portions of crystal mush.

1335

1336 **Figure 12:** Plot showing the time required to segregate 0.01 km³ of crystal poor pantellerite (black lines) and
1337 metaluminous rhyolite (grey lines) from crystals by compaction (solid lines) and hindered settling (dashed lines) as a
1338 function of the grain size. An example crystal size distribution for a typical Aluto pantellerite post-caldera lava is
1339 shown above.

Figure 1.

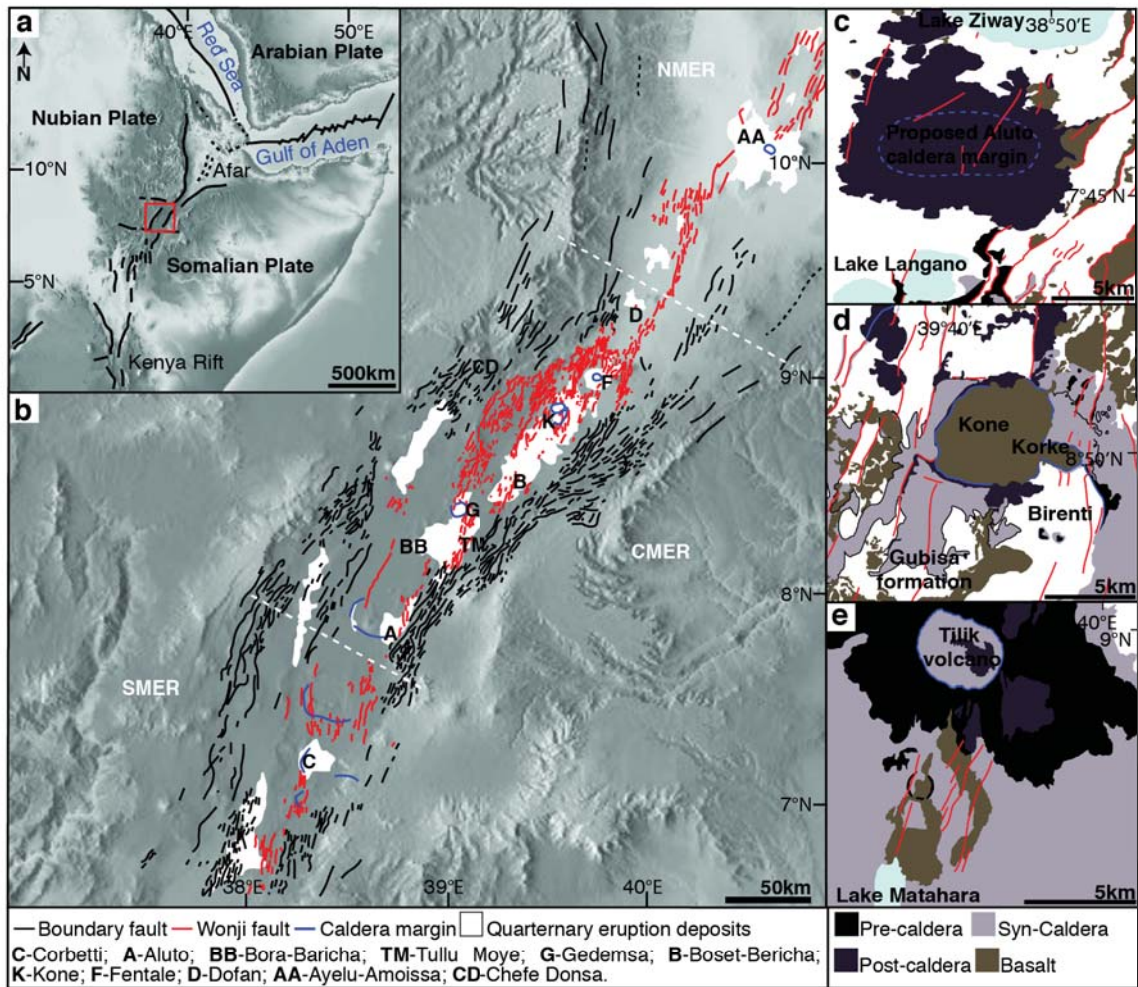


Figure 2.

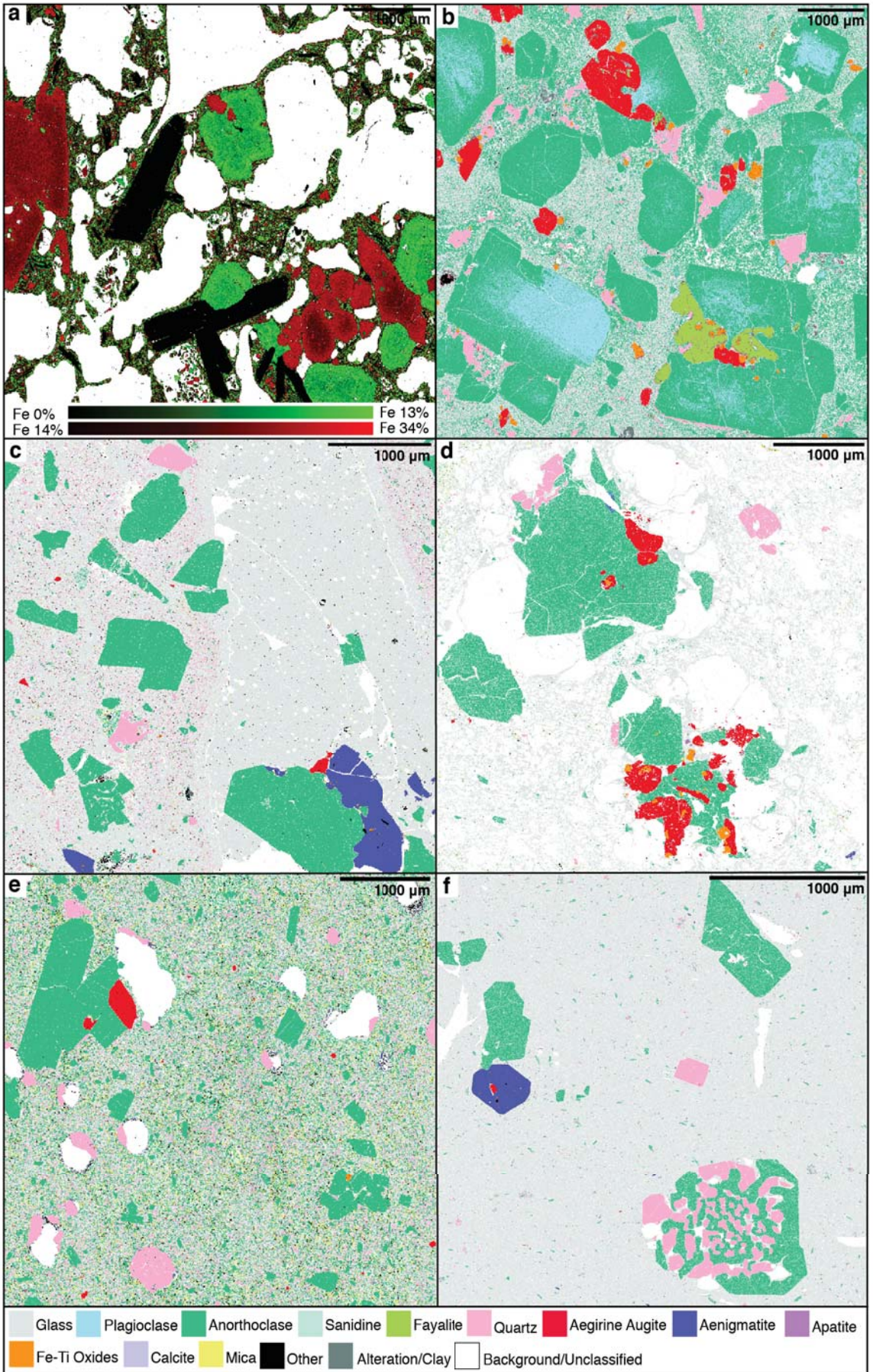
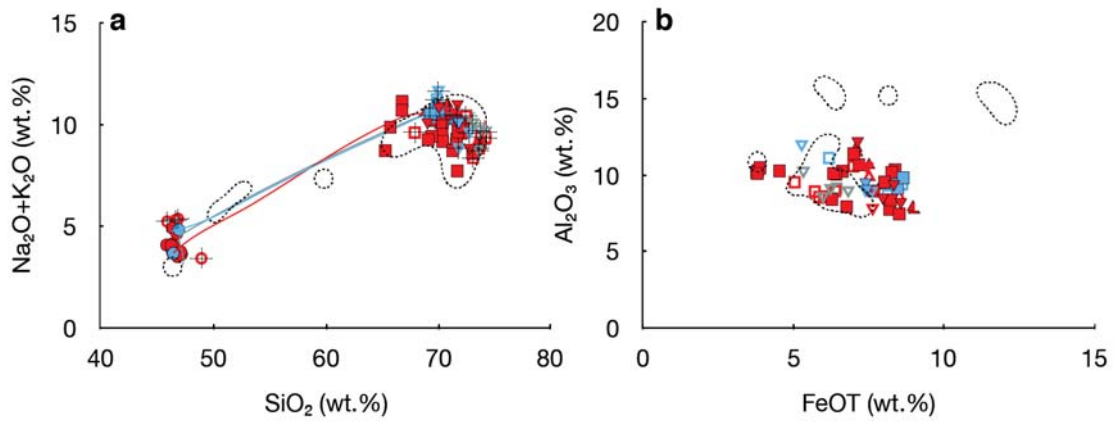
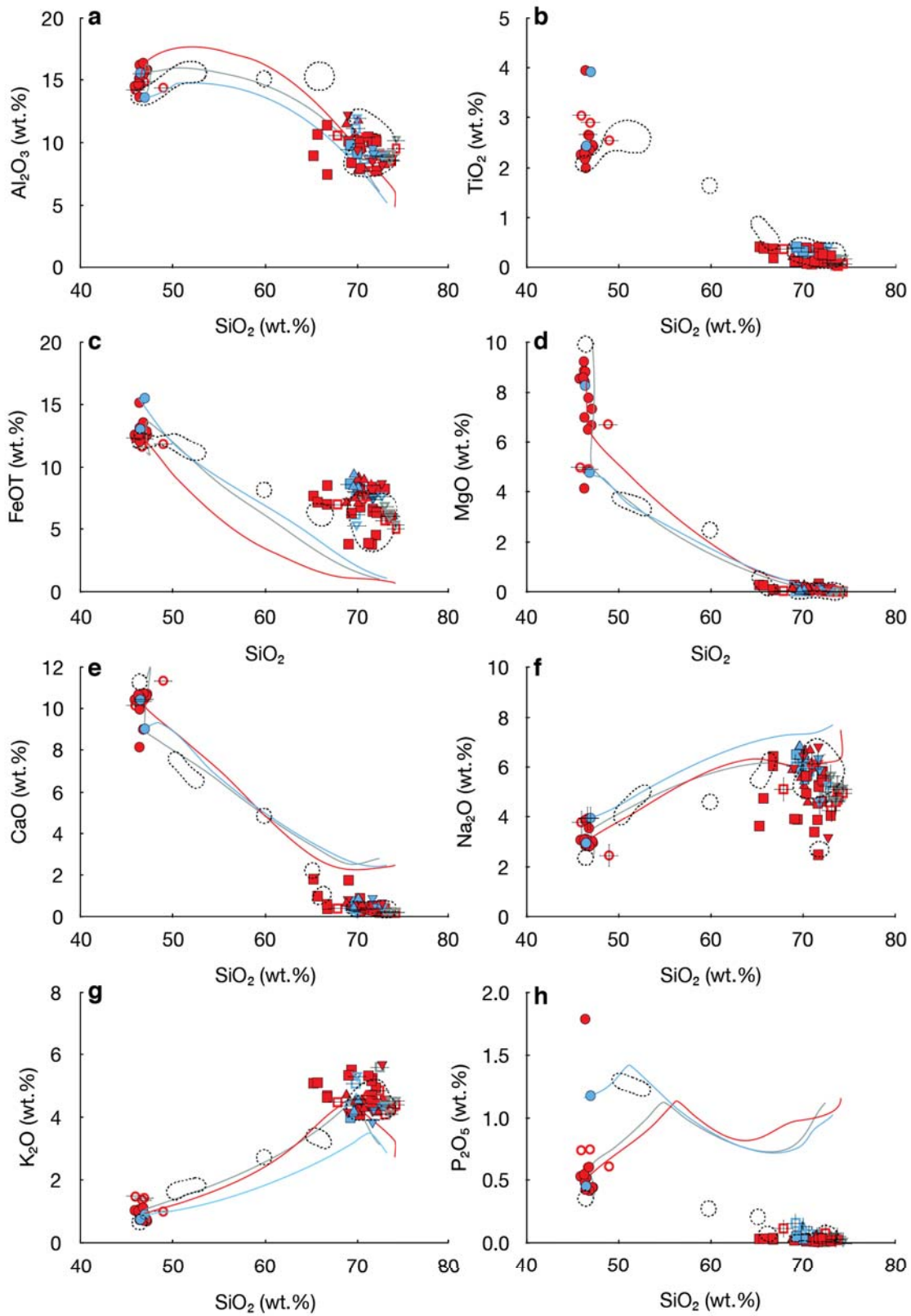


Figure 3.



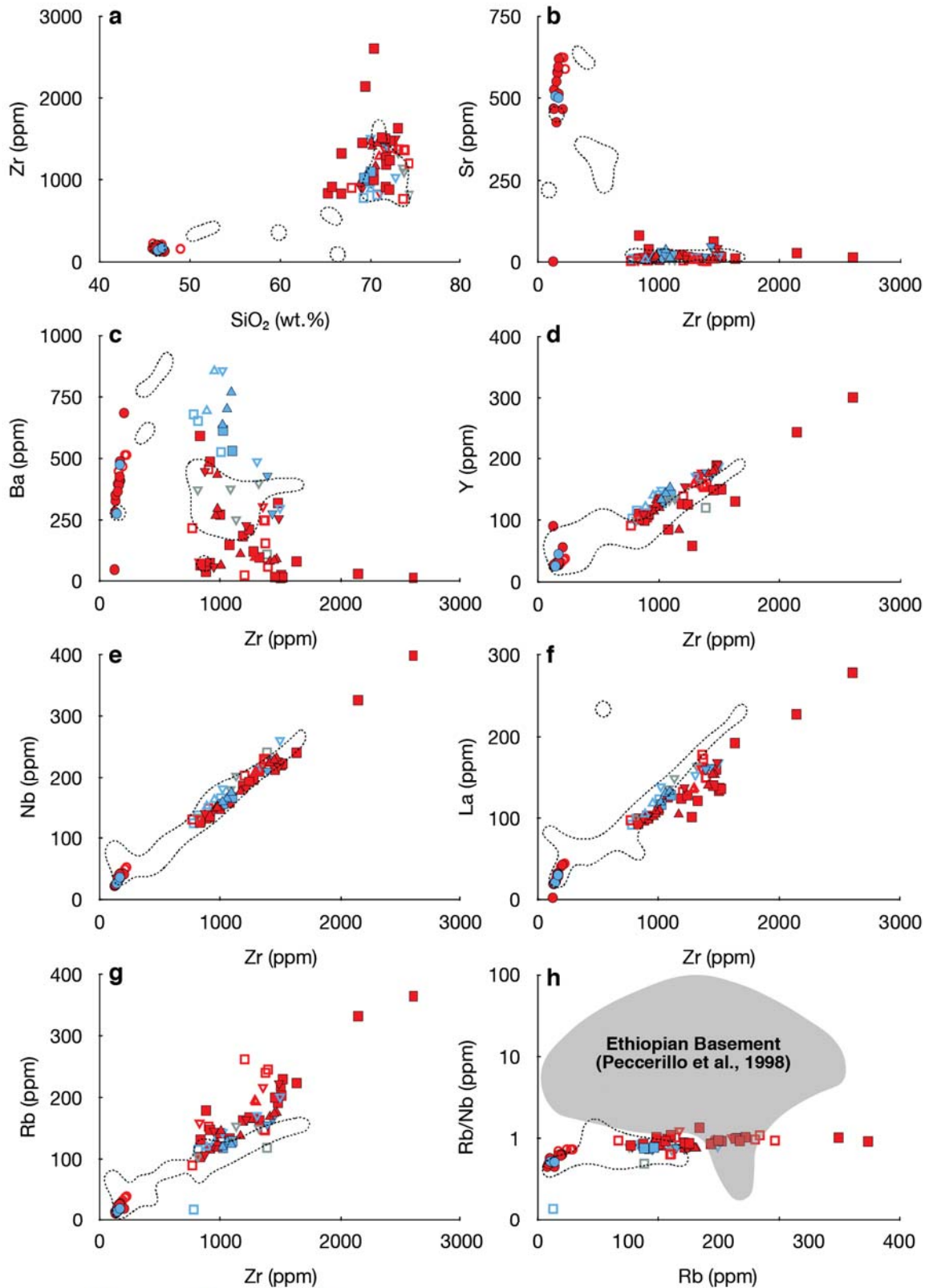
- Kone ● Fentale ● Aluto
- Post-caldera mafic (WR) ○ Post-caldera mafic (glass)
- ▼ Post-caldera silicic (WR) ▼ Post-caldera silicic (glass)
- Caldera (WR) □ Caldera (glass)
- ▲ Pre-caldera (WR) ▲ Pre-caldera (glass)
- Kone best fit RhyoliteMELTS model (100MPa, QFM+1, 1wt% H₂O)
- Fentale best fit RhyoliteMELTS model (100MPa, QFM, 1wt% H₂O)
- Aluto best fit RhyoliteMELTS model (Gleeson et al., 2017- 100MPa, QFM, 0.5wt% H₂O)
- Aluto WR range (Hutchison et al., 2016c)

Figure 4.



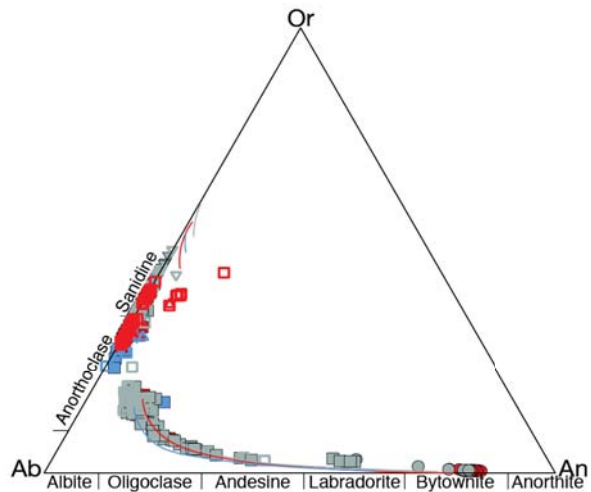
- Kone ● Fentale ● Aluto
- Post-caldera mafic (WR) ○ Post-caldera mafic (glass)
- Post-caldera silicic (WR) ▼ Post-caldera silicic (glass)
- Caldera (WR) □ Caldera (glass)
- ▲ Pre-caldera (WR) ▲ Pre-caldera (glass)
- Kone best fit RhyoliteMELTS model (100MPa, QFM+1, 1wt% H_2O)
- Fentale best fit RhyoliteMELTS model (100MPa, QFM, 1wt% H_2O)
- Aluto best fit RhyoliteMELTS model (Gleeson et al., 2017- 100MPa, QFM, 0.5wt% H_2O)
- Aluto WR range (Hutchison et al., 2016c)

Figure 5.



- Kone ● Fentale ● Aluto
- Post-caldera mafic (WR) ○ Post-caldera mafic (glass)
- ▼ Post-caldera silicic (WR) ▼ Post-caldera silicic (glass)
- Caldera (WR) □ Caldera (glass)
- ▲ Pre-caldera (WR) ▲ Pre-caldera (glass)
- Kone best fit RhyoliteMELTS model (100MPa, QFM+1, 1wt% H₂O)
- Fentale best fit RhyoliteMELTS model (100MPa, QFM, 1wt% H₂O)
- Aluto best fit RhyoliteMELTS model (Gleeson et al., 2017- 100MPa, QFM, 0.5wt% H₂O)
- Aluto WR range (Hutchison et al., 2016c)

Figure 6.



- Kone ● Fentale ● Aluto
- ▼ Post-caldera silicic (core) ▼ Post-caldera silicic (rim)
- Caldera (core) □ Caldera (rim)
- ▲ Pre-caldera (core) ▲ Pre-caldera (rim)
- Kone best fit RhyoliteMELTS model (100MPa, QFM+1, 1wt% H₂O)
- Fentale best fit RhyoliteMELTS model (100MPa, QFM, 1wt% H₂O)
- Aluto best fit RhyoliteMELTS model (Gleeson et al., 2017- 100MPa, QFM, 0.5wt% H₂O)

Figure 7.

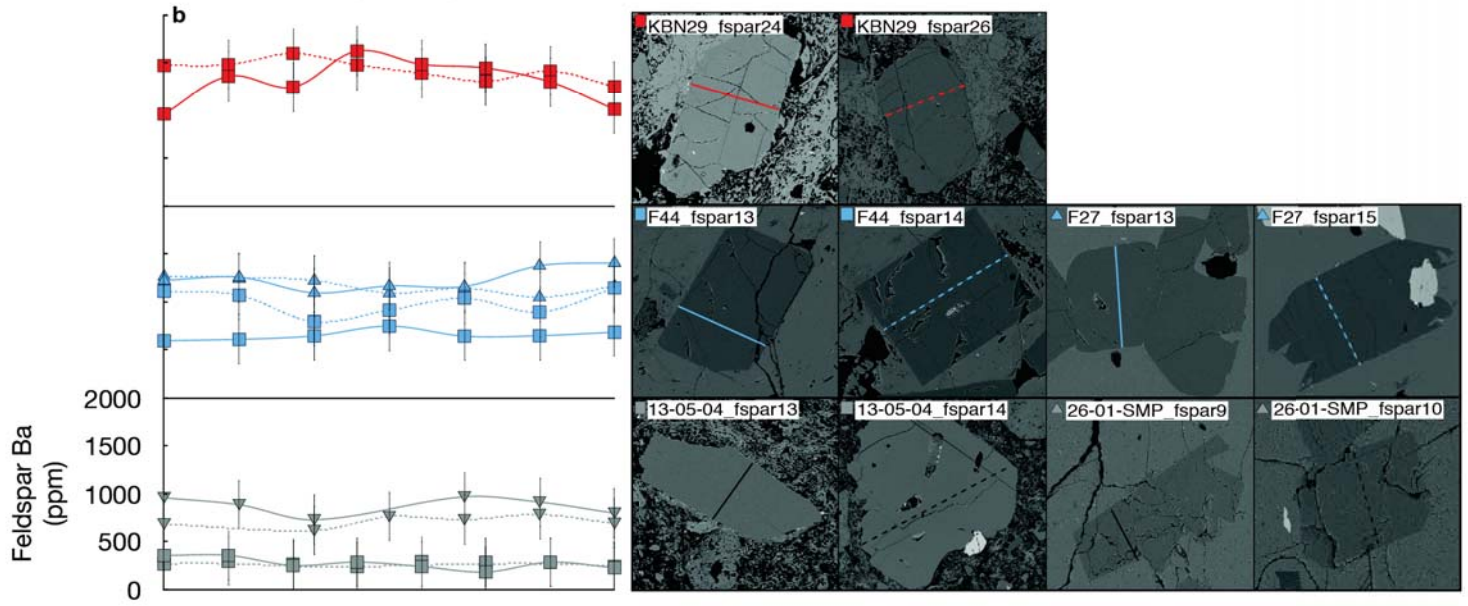
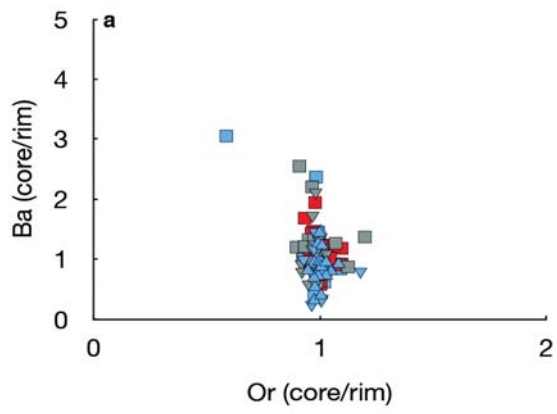
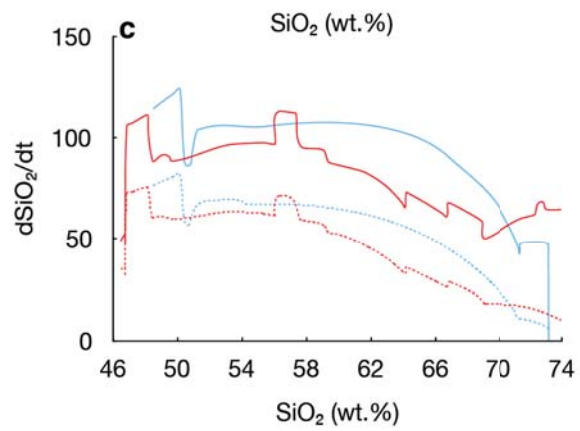
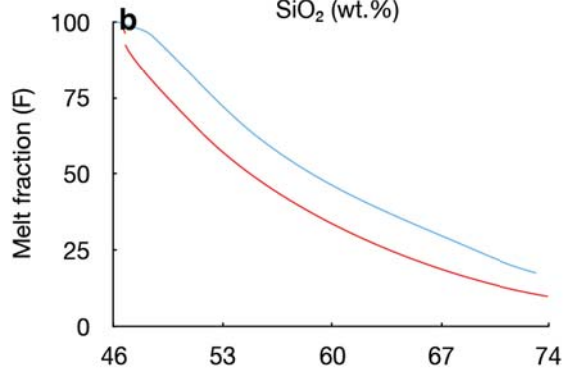
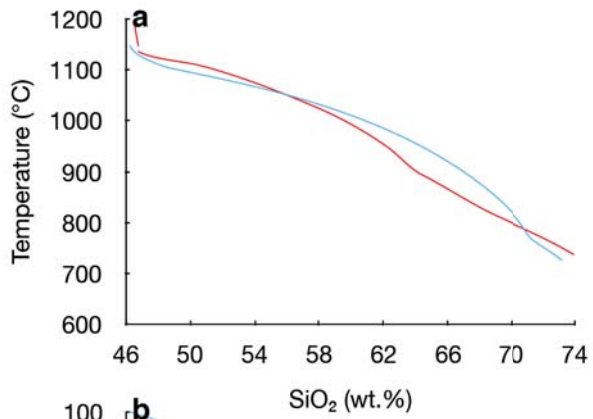
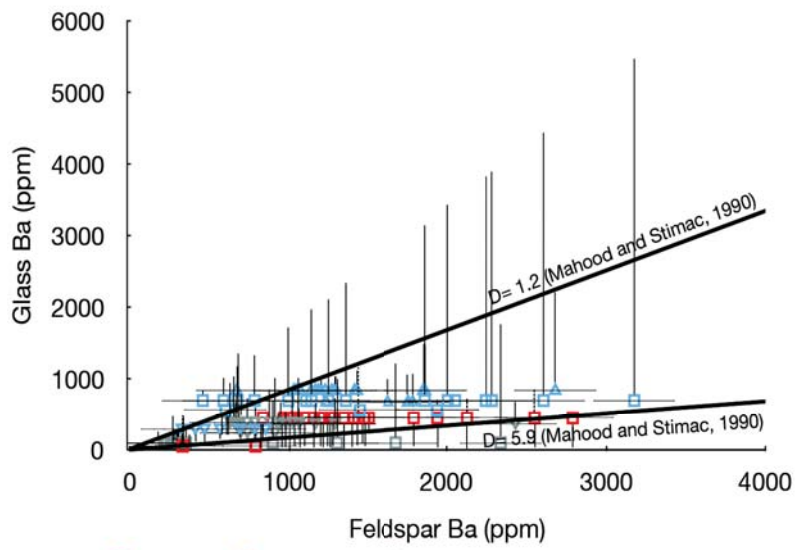


Figure 8.



- Kone best fit RhyoliteMELTS model (100MPa, QFM+1, 1wt% H₂O)
- Fentale best fit RhyoliteMELTS model (100MPa, QFM, 1wt% H₂O)

Figure 9.



- Kone ● Fentale ● Aluto
- ▼ Post-caldera silicic (core) ▼ Post-caldera silicic (rim)
- Caldera (core) □ Caldera (rim)
- ▲ Pre-caldera (core) ▲ Pre-caldera (rim)
- Predicted glass Ba (Henderson and Pierozynski, 2012)
- - - Adjusted predicted glass Ba (Henderson and Pierozynski, 2012)
- Mahood and Stimac, 1990

Figure 10.

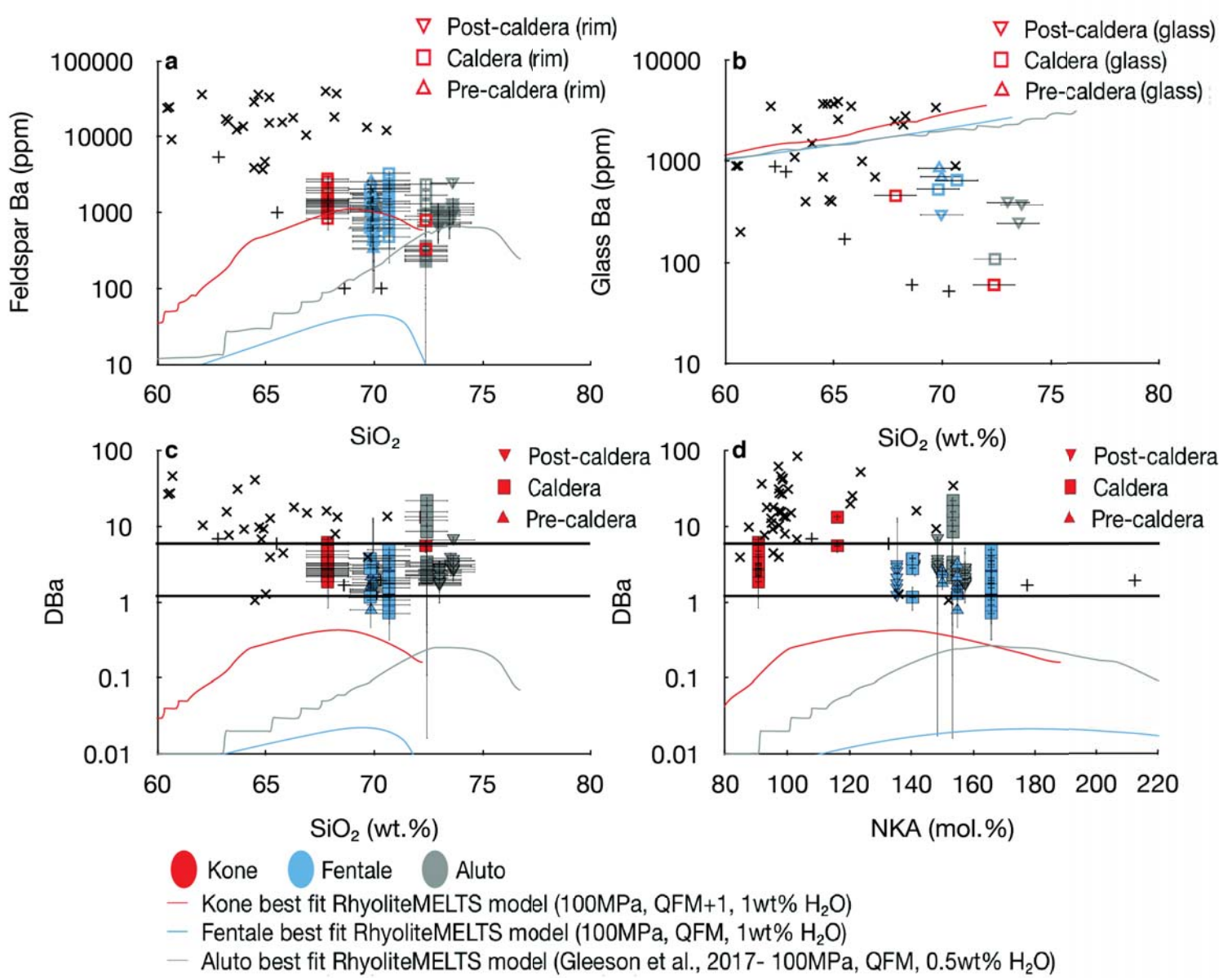


Figure 11.

Caldera Forming Eruptions

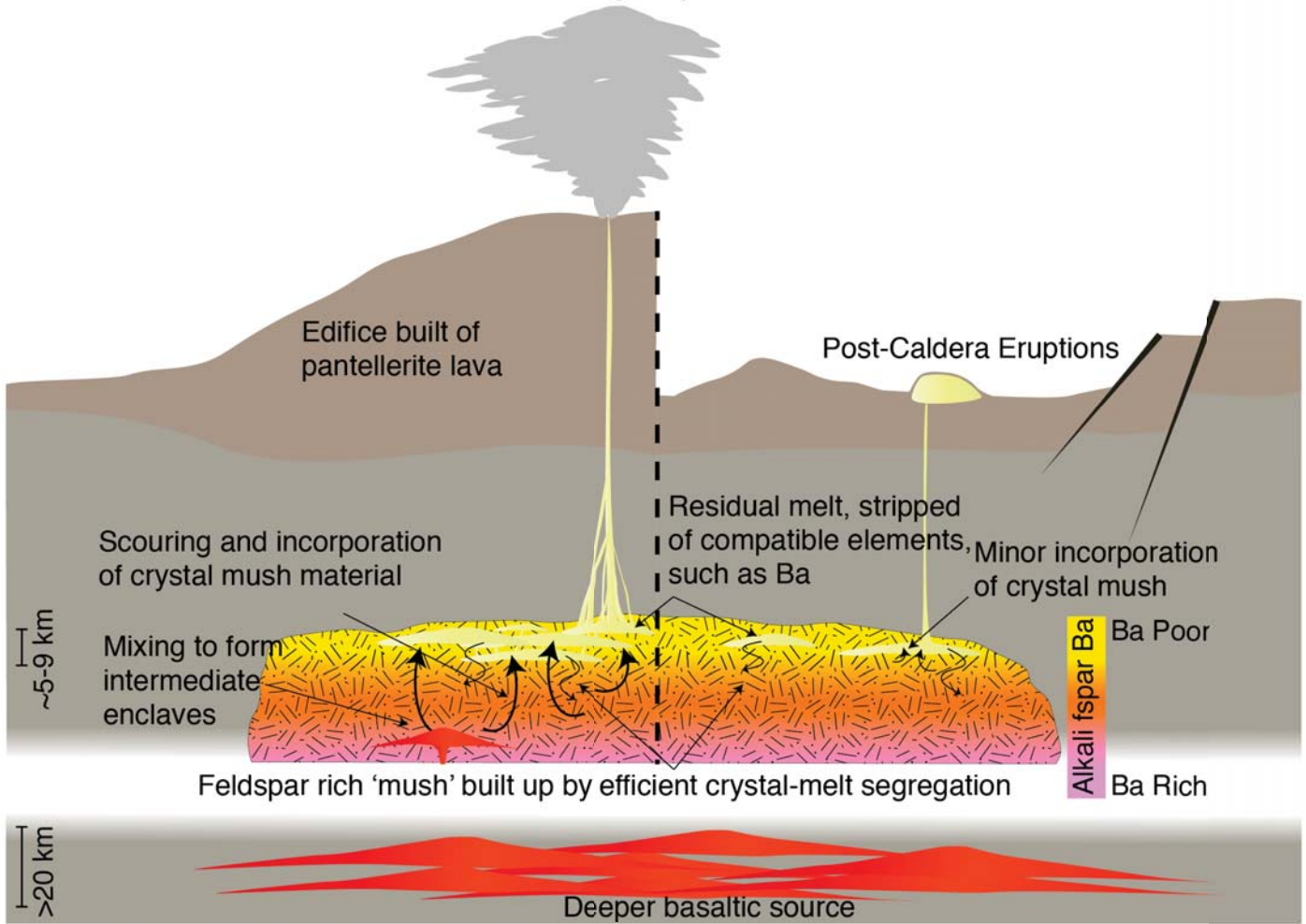


Figure 12.

